ARTICLES
https://doi.org/10.1038/s41593-021-00865-x

nature neuroscience

Check for updates

Collicular circuits for flexible sensorimotor routing

Chunyu A. Duan[1,2,3,7]✉, Marino Pagan[2,7], Alex T. Piet[2,4,7], Charles D. Kopec[2], Athena Akrami[2,3,5], Alexander J. Riordan[2], Jeffrey C. Erlich[2,6] and Carlos D. Brody[2,5]✉

Context-based sensorimotor routing is a hallmark of executive control. Pharmacological inactivations in rats have implicated the midbrain superior colliculus (SC) in this process. But what specific role is this, and what circuit mechanisms support it? Here we report a subset of rat SC neurons that instantiate a specific link between the representations of context and motor choice. Moreover, these neurons encode animals' choice far earlier than other neurons in the SC or in the frontal cortex, suggesting that their neural dynamics lead choice computation. Optogenetic inactivations revealed that SC activity during context encoding is necessary for choice behavior, even while that choice behavior is robust to inactivations during choice formation. Searches for SC circuit models matching our experimental results identified key circuit predictions while revealing some a priori expected features as unnecessary. Our results reveal circuit mechanisms within the SC that implement response inhibition and context-based vector inversion during executive control.

Our response to the sensation of our phone ringing will be very different in the context of having just heard 'the play is beginning; please silence all phones' versus a context in which we have just been told 'your child's school is about to call with urgent information'. Such top-down flexible switching in sensorimotor routing is central to our daily lives and is a core component of executive function[1]. One prominent paradigm to investigate executive function in the laboratory is the Pro/Anti task-switching behavior[2]. In this paradigm, subjects switch between two sensorimotor mappings: the 'Pro' task requires subjects to orient toward a peripheral target for reward, whereas the 'Anti' task requires subjects to orient away from a peripheral target. In humans, monkeys and rats, subjects display behavioral asymmetries between Pro and Anti responses: performance on Anti trials is slower and less accurate; and switching from Anti to Pro leads to a greater performance cost than switching from Pro to Anti[3–5]. These behavioral asymmetries suggest that the Pro task is more reflexive, whereas the Anti task is more cognitively demanding and requires response inhibition[5]. Selective impairment on the Anti task but not on the Pro task has been associated with failures of executive functions in patients with various psychiatric disorders[6,7]. These failures can be attributed either to an inability to inhibit the automatic and reflexive Pro responses (response inhibition) or to an inability to remap sensory input to the appropriate volitional motor response (vector inversion)[5,8].

Neural mechanisms underlying the Pro/Anti task-switching behavior have been extensively investigated in non-human primates[5,9]. A prevailing hypothesis has been that response inhibition is, in part, achieved by prefrontal cortical (PFC) inhibition of the SC[5], with the latter considered to be largely a spatiomotor structure[10–15]. This hypothesis would predict that silencing PFC would disinhibit collicular activity. However, silencing primate PFC was found to, instead, reduce activity in the SC[16]. Moreover, in a recently developed Pro/Anti orienting behavior in rats, pharmacological inactivation of the SC led to selective impairment of the cognitively demanding Anti task while sparing the Pro task[3]. These data suggest a more cognitive role for the SC in executive function than previously appreciated—a proposal that aligns with recent studies that put forth more integrative roles of the SC in target selection, spatial attention and decision-making[17–22]. If the SC plays a cognitive role in the Pro/Anti behavior, what specific role is this? Is the SC involved in the computation that combines context information with sensory information to produce appropriate choices? Or is the SC simply a part of the motor output pathway but specifically during Anti trials? And what circuit mechanisms underlie the SC's role in the behavior? It is notable that executive control behaviors have several distinct task epochs, requiring distinct computations. Nevertheless, no neural perturbations with sub-trial temporal resolution have yet been reported during executive control. This has made it difficult to causally link brain regions to specific computational roles in the behavior.

In this study, using a rat Pro/Anti behavior, we employed sub-trial optogenetic perturbations, electrophysiological recordings and computational modeling of SC circuits to address these questions. We identified a key subset of SC neurons, distinguished by their response timing and their relationship to behavior, that link context representation to choice representation. These neurons appear to lead the computation that combines task context with the sensory stimulus to produce the subject's choices. Temporally specific SC inactivations demonstrated that SC activity during the context-encoding period is causally required for behavior. We were surprised to find that behavior is much more robust to SC inactivations during the choice formation period. However, models of SC neural dynamics built with a structure based on our electrophysiological findings, and trained to reproduce our optogenetic data, show that this is, nonetheless, consistent with choice computation occurring in, and being led by, the SC. Large-scale computational searches of these SC circuit models revealed which features of within-SC connectivity are necessary to replicate our experimental data and also identified some a priori expected features that turned out to be irrelevant. Taken together, our data and models identify key circuit mechanisms underlying response inhibition and

[1]Institute of Neuroscience, State Key Laboratory of Neuroscience, CAS Center for Excellence in Brain Science and Intelligence Technology, Chinese Academy of Sciences, Shanghai, China. [2]Princeton Neuroscience Institute, Princeton University, Princeton, NJ, USA. [3]Sainsbury Wellcome Centre, UCL, London, UK. [4]Allen Institute for Brain Science, Seattle, WA, USA. [5]Howard Hughes Medical Institute, Princeton University, Princeton, NJ, USA. [6]NYU-ECNU Institute of Brain and Cognitive Science, NYU Shanghai, Shanghai, China. [7]These authors contributed equally: Chunyu A. Duan, Marino Pagan, Alex T. Piet. ✉e-mail: c.duan@ucl.ac.uk; brody@princeton.edu

context-based vector inversion that support a leading role for the SC during executive control.

Results

We trained rats to perform task switching in a behavior in which two different task contexts require opposite sensorimotor orienting responses[3] (Fig. 1a). On each trial, rats are first presented with a non-spatial auditory cue indicating the task context for the current trial (labeled 'Pro' or 'Anti'). This is followed by a silent delay period and then by a spatial choice period during which a visual stimulus to one side is turned on; in the Pro context, rats are required to orient toward it, whereas, in the Anti context, they should orient away (Fig. 1b). We used easily distinguishable Pro and Anti cue stimuli. Our focus here was not on the animal's decision as to which of the Pro versus Anti context it is in. Instead, our focus was on how that non-spatial context information, held in memory, is combined with the spatial cue information provided by the side light. It is only after that side light is presented that the subject's spatial choice can begin to be formed. We refer to the period between side light onset and the animal's choice as the 'choice period'. This includes both the cognitive process of combining context and sensory cue information to form a choice and the potentially overlapping response process of implementing that choice. Similarly to previous results[3,5], rats displayed multiple behavioral asymmetries between Pro and Anti responses (Extended Data Fig. 1). These asymmetries indicate the Pro task as a stimulus-driven task, whereas the Anti task is more cognitively demanding.

In the electrophysiological and optogenetic experiments, the Pro/Anti task contexts were presented in blocks of trials, with context being cued on each trial, remaining constant within a block and alternating between blocks. We varied the block duration (mean ± s.d. = 24.3 ± 9.0 trials) so that rats could not predict when the task context switched. As observed previously[3], the change in performance on the first trial of each block implied that rats were monitoring each trial's task context cue (Extended Data Fig. 1d). Within-block trials were far more common in our dataset than context-switching trials, and we focus exclusively on within-block trials below.

SC and PFC populations encode task context and motor choice. To investigate neural representations in collicular and frontal cortical regions previously implicated in task switching[3,23], we recorded single units in the deep layers of the SC and in the prelimbic region of the medial PFC (Extended Data Fig. 2a, Supplementary Fig. 1 and Methods). We analyzed neurons for which we had collected responses during at least 25 correct trials for each of the four task conditions (Pro-Go-Right, Pro-Go-Left, Anti-Go-Right and Anti-Go-Left). This resulted in the analysis of 193 SC neurons (out of 215; Fig. 1) and 291 PFC neurons (out of 331; Extended Data Fig. 3). Unless otherwise noted, all analyses were performed on correct trials, and trial numbers were balanced across four conditions (25 trials per condition).

Individual neurons in SC and PFC encoded task context (Pro or Anti) as well as the subsequent spatial choice (Left or Right; Fig. 1c–e, Extended Data Fig. 3 and Supplementary Fig. 2). We quantified each neuron's selectivity by computing d', a measure of the separation between two response distributions, at each time point for the two task contexts and, separately, for the two choices (Methods and Supplementary Fig. 3). In both SC and PFC, we observed neurons that preferred Pro or Anti task trials (Fig. 1c, Extended Data Fig. 3a and Methods) and neurons that were selective for orienting responses ipsilateral (ipsi) or contralateral (contra) to the recorded side[10,24] (Fig. 1e and Extended Data Fig. 3c). Consistent with previous studies[10], many SC neurons were side selective until entry into the response side port, suggesting a role in motor execution (Supplementary Fig. 4). These features are preserved in neurons recorded from individual rats (Extended Data Fig. 4). Also consistent with previous findings in rodent SC[10], no statistically significant difference was found between the number of ipsi-preferring and contra-preferring neurons (in SC, 40%, 77/193 contra-preferring and 35%, 68/193 ipsi-preferring; $P = 0.34$, chi-squared test).

In contrast to past studies of the SC using delayed response tasks[22,25,26], the encoding of Pro/Anti task context here is dissociated from motor planning, as supported by a lack of side-selective activity before the choice period (Fig. 1e). Therefore, the Pro/Anti selectivity observed during the task context cue and delay period could not be attributed to a lateralized or visually related encoding strategy. Analysis of the animals' head orientation angles did not reveal a significant difference between Pro and Anti trials during the delay period, suggesting that rats did not use an overt embodied strategy to encode context (Supplementary Fig. 5 and Methods). Nevertheless, we do not rule out that rats could have encoded task context using unobserved muscle activation.

Recordings in primate SC neurons have reported higher activity associated with visually guided responses compared to non-visually guided responses[27]. We compared population-averaged firing rates on Pro (visually guided) versus Anti (non-visually guided) trials during this choice period (0–250 ms after light onset) and found no significant difference between average firing rates on Pro (18.11 ± 0.03 Hz) versus Anti (17.84 ± 0.03 Hz) trials in the SC population ($n = 193$; $P = 0.10$). Therefore, even during the choice period, Pro versus Anti firing rate differences were not the result of an overall difference between visually guided versus non-visually guided responses. Finally, the Pro/Anti selectivity observed in individual SC neurons during the choice period did not simply reflect a motor execution signal: Pro/Anti d' values persisted even when ipsilateral and contralateral orienting trials were analyzed separately (Supplementary Fig. 6a).

Similarly to observations in prefrontal cortical regions during cognitive tasks[23,28,29] (Extended Data Fig. 3), the encoding in SC appeared to be multiplexed and highly heterogeneous across different neurons[26,27] (Fig. 1c–e). An initial inspection of the entire SC population revealed no apparent correlation between task context and choice preference (Extended Data Fig. 5a) or clear temporal order of Pro versus Anti task context selectivity. Given the heterogeneous and multiplexed nature of single-neuron responses (Fig. 2a and Supplementary Fig. 7a), we focused on the representation of task variables at the population level (Fig. 2).

To evaluate the amount of task context information in SC and PFC populations, we used a cross-validated linear decoding approach to classify Pro versus Anti responses or Left versus Right responses in neural population space[30] (Methods). We included all the neurons for this analysis (193 SC neurons and 291 PFC neurons) but matched the number of neurons from different brain areas ($n = 193$; Methods). Similarly to task context information in the PFC population (Supplementary Fig. 7b), decoding for whether a trial was Pro or Anti was significantly above chance in the SC population throughout the trial duration (Fig. 2b), even when analyzed separately for ipsilateral versus contralateral choices (Supplementary Fig. 6b). After the onset of side light stimulus, Left versus Right choice information emerged in SC with short latency (Fig. 2c; latency = 49 ± 18 ms), significantly earlier than that in PFC (latency difference = 186 ± 24 ms; $P = 10^{-3}$, non-parametric permutation test). This choice information latency difference is not a result of differences between the two populations in firing rate, overall strength of d' or number of neurons (Supplementary Fig. 8). We also recorded neurons in the rat frontal orienting fields (FOF) ($n = 429$ neurons) from a slightly different version of the Pro/Anti task (Methods) and found that the appearance of choice information in SC was also significantly earlier than that in FOF (Fig. 2c; latency difference = 222 ± 29 ms; $P = 10^{-3}$, permutation test). Although we cannot rule out that other cortical regions might

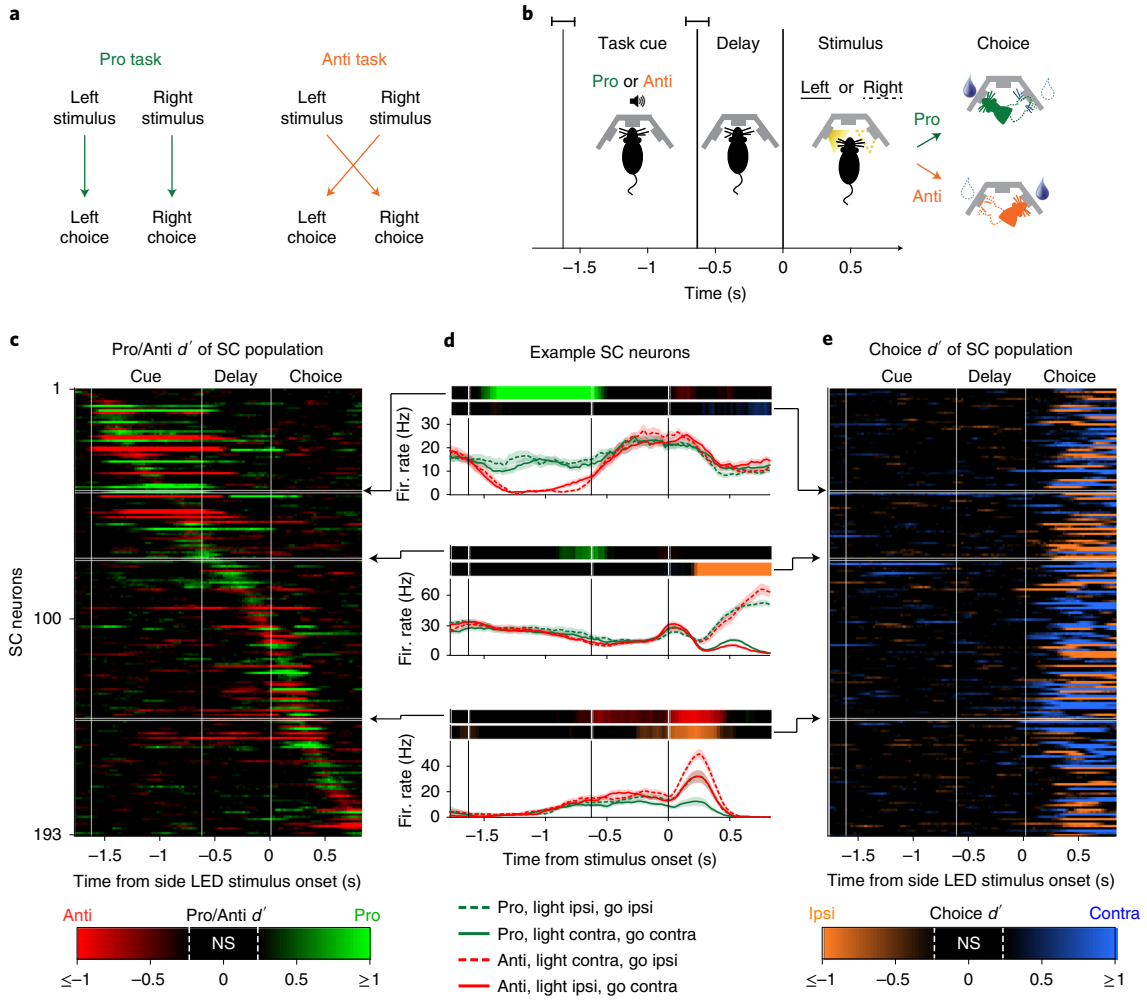

Fig. 1 | Individual SC neurons encode task and choice variables during flexible sensorimotor routing. a, Rules for the Pro and Anti task contexts. In the Pro task, rats should orient toward a lateralized stimulus (left or right) for reward; in the Anti task, rats should orient away from the stimulus for reward. Trained rats can switch between these two known task contexts. **b**, Rats nose-poke in the center port to initiate each trial and keep fixation during a 1-s task cue (Pro or Anti sound) and a 0.5-s delay period. After the delay ends, the animal is allowed to withdraw from the center port (mean time between delay end and animal's withdrawal = 127 ms). The withdrawal triggers the onset of a lateralized LED light (left or right) to indicate the stimulus location. Rats then poke into one of the side-pokes for reward. Trials are aligned to light stimulus onset (time 0), and the vertical lines and horizontal error bars indicate the mean and the 20th and 80th percentiles of task cue onset and delay onset times (Methods; the variability is introduced by the animal's variable time between delay end and center port withdrawal; for analysis aligned to side response, see Supplementary Fig. 4). These variable time indicators on task cue and delay onset apply to all subsequent plots but are omitted from them for simplicity. **c**, Matrix of Pro/Anti selectivity for the SC population (193 of 215 total neurons). Each row of the matrix represents the Pro/Anti signed d' of a single neuron as a function of time. Neurons are sorted by the timing of their peak Pro/Anti absolute d'. Only correct trials were included in this analysis. d' values that are not significant (NS) have their color code set to 0 (black). For **c**–**e**, analysis is on sliding windows of width = 250 ms, placed such that each window includes spikes from −250 to 0 ms relative to the plotted time point. **d**, Peri-stimulus time histogram (PSTH) for three example SC neurons on Pro-Go-Contra (green solid), Pro-Go-Ipsi (green dashed), Anti-Go-Contra (red solid) and Anti-Go-Ipsi (red dashed) trials (mean ± s.e.m.). PSTHs are aligned to stimulus onset. Top: Pro/Anti signed d' and Go Ipsi/Contra signed d' as a function of time for each neuron. d' values that are NS have their color code set to 0 (black); two-sided t-tests, threshold $P = 0.05$. None of these representative examples had statistically significant linearly decodable information about which side the light stimulus was on: the maximum d' values for light side information for the three neurons, from top to bottom, were 0.19 ($P = 0.56$), 0.26 ($P = 0.28$) and 0.13 ($P = 0.79$). **e**, Matrix of choice (Go Ipsi/Go Contra) selectivity for the SC population. The recorded hemisphere was randomly assigned for each rat. We, therefore, quantified choice selectivity as preference for orienting responses ipsilateral or contralateral to the recorded side. Neurons are sorted as in **c**. Fir, firing.

encode spatial choice even faster than the SC, these results suggest that the SC might play a leading role in forming the spatial decision. Compared to the strong and early information in the SC deep layers about the animal's upcoming orienting choice, sensory information regarding which side the light stimulus was on was significantly weaker ($P = 10^{-3}$, t-test) and appeared significantly later (latency difference = 191 ± 33 ms; $P = 10^{-3}$, permutation test; Extended Data Fig. 6), a result consistent with the role of SC deep layers in motor processes[11,17].

A subset of SC task-encoding neurons are linked to decisions. A closer examination of SC neurons revealed subpopulations that encode distinct types of information (Fig. 3). For each SC neuron, we computed the temporal profile of significant task context

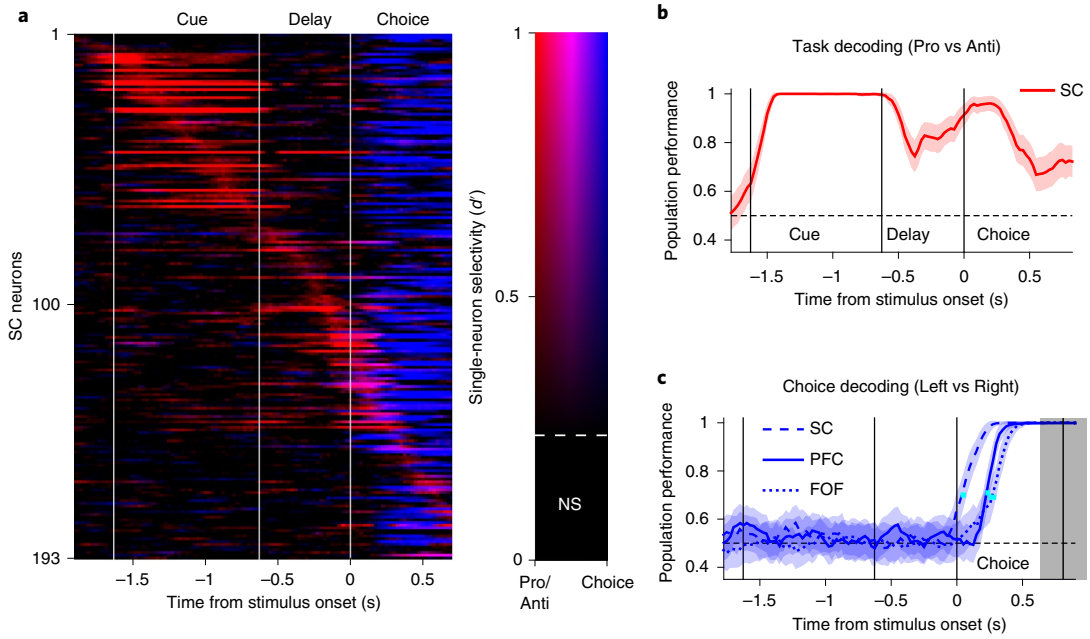

Fig. 2 | SC population contains strong task context information and earlier choice information than prefrontal cortical populations. a, Multiplexed task context and choice encoding in the SC population. Similarly to Fig. 1c–e, but, instead of focusing on the sign of task context and choice preference, the strength of task context and choice selectivity are simultaneously illustrated here for each neuron to demonstrate multiplexing. The intensity of the color represents how 'informative' a neuron is, and the RGB values are associated with different types of information (Pro/Anti, red; choice, blue; mixed, purple). *d′* values that are not significant (NS) are set to 0 and displayed as black. **b**, Mean ± s.d. performance for linear classification of correct Pro versus Anti trials for the SC population (193 neurons). Spikes are aligned to stimulus onset and counted over windows of 250 ms with 25-ms shifts between neighboring windows. Note that performance is plotted over the right edge of the window (causal). **c**, Classification performance to linearly separate Go-Left versus Go-Right trials for equally sized SC (dashed), PFC (solid) and FOF (dotted) population ($n = 193$ neurons). Shaded area indicates the median ± s.d. of animals' RT (800.5 ± 362.9 ms). Horizontal cyan error bars represent mean ± s.d. of the timing of reaching 0.7 decoding accuracy for each population. RGB, red, green, blue.

selectivity (Pro versus Anti) and ranked neurons by the time of their peak selectivity (Fig. 3a). Although there is a continuum of selectivity timings (Supplementary Fig. 9), for analysis purposes we divided the SC neurons into two broad subpopulations according to when they encoded Pro/Anti information. One group of SC neurons ('cue neurons', cyan) differentiated between Pro and Anti trials most strongly during the auditory cue, whereas another subpopulation represented task context most strongly when the auditory cue was no longer present ('delay/choice neurons', yellow). The representation of task context by cue neurons was progressively weakened after the end of the cue, and it did not differentiate between correct and error trials (Fig. 3b, top), consistent with these neurons carrying a purely sensory signal with little relationship to behavior.

In contrast, three lines of evidence suggest that the SC delay/choice neurons (which have both Pro versus Anti and contra versus ipsi preferences) play a key role in behavior. First, their task context information slowly ramped up throughout the cue presentation and the delay, peaking at the time when rats were required to make a decision (Fig. 3b, bottom, solid line). Second, this representation was significantly disrupted on error trials during the delay and choice periods (Fig. 3b, bottom, dashed line; $P = 10^{-3}$, *t*-test), indicating a strong correlation with behavior. Third, when decoded for contra versus ipsi choices, these neurons contained an early representation of choice, substantially and significantly faster than the SC cue neurons or the PFC or FOF neurons (Fig. 3c; SC delay/choice neurons = 84 ± 19 ms; SC cue neurons = 196 ± 38 ms; PFC neurons = 290 ± 34 ms, $P = 10^{-3}$, permutation test; FOF neurons (not shown in Fig. 3c for plot clarity) = 342 ± 39 ms, $P = 10^{-3}$, permutation test; $n = 29$ neurons in each of the four groups; also see Supplementary Fig. 10).

In our behavior, it is immediately after the visual target onset that animals apply the non-spatial task context (Pro or Anti) to form their spatial orienting choice (ipsilateral or contralateral to the recorded side). We, therefore, focused on a time window immediately after visual target onset, and on the delay/choice neurons, to examine how task context and choice signals were multiplexed (Fig. 4). In contrast to the heterogeneity initially observed in the entire SC population (Fig. 1c–e), this focus revealed a systematic relationship between each neuron's task context selectivity and choice selectivity (Fig. 4 and Extended Data Fig. 5b). SC delay/choice neurons that were significantly Contra-preferring during this time window (that is, neurons having a P value < 0.05, *t*-test; Methods) tended to also be Pro-preferring (Fig. 4a), whereas SC delay/choice neurons that were significantly Ipsi-preferring tended to also be Anti-preferring (Fig. 4c). Although there was a continuum of selectivity (Fig. 4b), we refer to the two predominant types at the ends of the spectrum as Pro/Contra-preferring neurons and Anti/Ipsi-preferring neurons. The predominance of Pro/Contra-preferring neurons and Anti/Ipsi-preferring neurons was not simply due to higher firing rate responses for visual stimuli from the contralateral side. Such a preference would have implied that individual neurons would have higher firing rates on both Pro/Contra and Anti/Ipsi trials. Instead, individual neurons were either Pro/Contra-preferring or Anti/Ipsi-preferring and had a complex, non-linear interaction between task context information and target location (see the Anti/Ipsi-preferring example in Fig. 1d, bottom, and the weak and late light stimulus information in the SC population in Extended Data Fig. 6).

SC activity is necessary during the non-spatial task-encoding delay period. Because different behavioral epochs of the task

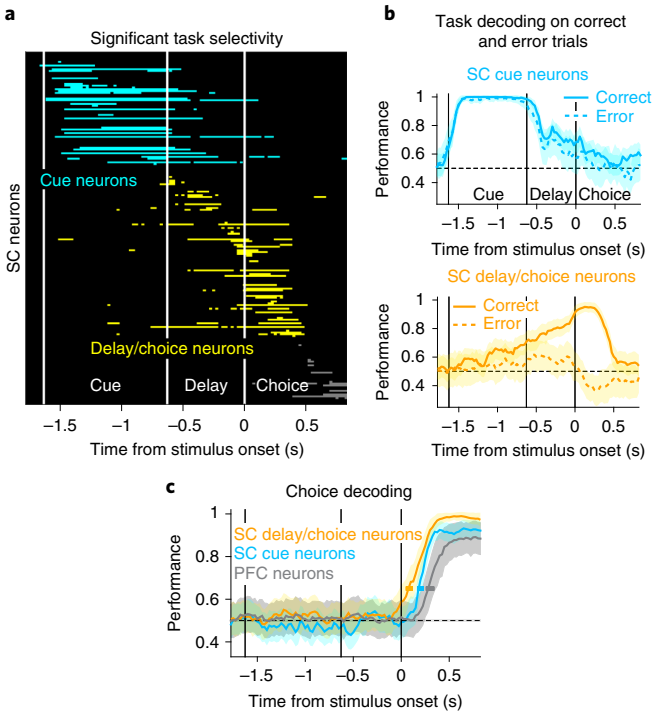

Fig. 3 | Distinct roles of SC subpopulations. a, Timing of significant Pro/Anti selectivity (d') for all SC neurons, sorted by peak d'. Significance threshold was determined by shuffled data. We separated SC neurons into two groups based on the timing of their Pro/Anti selectivity. 'Cue neurons' (cyan, $n=29$) differentiated between Pro and Anti trials most strongly during the auditory cue; 'delay/choice neurons' represented task context selectivity most strongly when the auditory cue was no longer present (yellow, $n=45$). **b**, Mean ± s.d. performance of task context decoding on correct versus error trials. Linear classifiers trained on correct trials were tested for separate correct trials (solid) or error trials (dashed). The representation of task context by delay/choice neurons was disrupted on error trials, whereas such information in the cue neurons did not differentiate between correct and error trials. **c**, Choice decoding performance of SC subpopulations and PFC neurons ($n=29$ in all three populations, to match number of cue neurons; Methods). Choice information emerged first in SC delay/choice neurons. Shaded areas (vertical error bars) indicate s.d. of decoding accuracy for each population across time. Horizontal error bars represent mean ± s.d. of the timing of reaching 0.65 decoding accuracy for each population.

require distinct computations, we selectively probed the requirement of SC activity during separate epochs[22,25,31] using bilateral optogenetic inactivation of SC neurons, mediated by virally expressed eNpHR3.0 (Fig. 5a,b, Supplementary Fig. 1c and Methods). Optogenetic inactivation that covered the entire trial period (3 s) of a randomly selected 25% of trials resulted in a selective Anti impairment on those trials (Fig. 5c and Extended Data Fig. 7a; permutation test, $P=4\times10^{-3}$ across animals or all trials). This replicates previous pharmacological inactivation results where SC activity was suppressed during the entire session[3]. Turning to temporally specific inactivations (detailed inactivation timing in Extended Data Fig. 2b), we found that bilateral SC inactivation during the task cue period did not result in any behavioral deficit (Fig. 5d, left), consistent with a sensory role for cue neurons that are not linked to correct performance (Fig. 3b). In contrast, bilateral SC inactivation during the delay epoch significantly increased error rates on Anti trials (Fig. 5d, middle; bootstrapped $P=8\times10^{-3}$). This suggests that an intact representation of task context, which is neither a spatial variable nor a motor variable, is required in the SC during the delay period for animals to perform the behavior. This finding is consistent with our electrophysiology data that linked SC delay/choice neurons to flexible sensorimotor behavior (Fig. 3b) but does not distinguish whether the required task context representation is generated within the SC or inherited from elsewhere. These delay period inactivation effects are unlikely to be due to an overlap between early processing of the visual stimulus and slow release from inactivation at the end of the delay period (full release reached ~60 ms after delay offset; Fig. 5b). The visual stimulus was presented only after subjects responded to the end of the delay by withdrawing from the center nose port, which, on average, occurred ~127 ms after delay offset (Extended Data Fig. 2b), long after the inactivation release had concluded. Finally, given the strong and early choice signal in the SC, we were surprised to find that bilateral choice period inactivation did not have any effect on choice accuracy (Fig. 5d, right; $P>0.05$), although we did observe an increase in reaction time (RT) on correct Anti responses (Extended Data Fig. 7b; RT increase = 22.5 ± 15.3 ms). This lack of effect on choice accuracy upon choice period inactivation might, at first sight, suggest that, in contrast to what the electrophysiological results implied, the SC is only a minor contributor to choice formation. However, computational efforts that we now describe revealed that even models in which the SC is solely responsible for choice formation can be fully compatible with our optogenetic and electrophysiological data.

Collicular models of executive control consistent with perturbation data. We used computational modeling to ask two main questions. First, is choice formation circuitry external to the SC necessary to explain the lack of behavioral impairment after choice period SC inactivation? Or could circuitry purely within the SC lead to both choice formation and the pattern of behavioral changes in our optogenetic experiments (Fig. 5d)? Second, if neural circuitry purely within the SC is indeed sufficient to account for the optogenetic data, what constraints do that data place on the circuitry? To address these questions, we used a simplified SC model framework, inspired by the electrophysiological data in Fig. 4, and focused on reproducing the data of Fig. 5d. As we describe below, this approach revealed a surprisingly diverse population of models consistent with the data[32–34].

The SC was represented by four pools of neurons: a Pro pool and an Anti pool on each side of the brain (Fig. 6a and Methods). Pro and Anti pools differed in strengths of connections with other pools in the model and in receiving opposite levels of excitation in Pro versus Anti trials. Given our experimental finding that Pro-preferring neurons had a strong tendency to be Contra-preferring neurons (Fig. 4b), and given that unilateral SC stimulation drives contralateral orienting motions[15,35], we took the Pro pool in the model as also being a Contra-preferring pool and as driving the motor output. The final choice of the model on each trial was determined by which of the two Pro/Contra units, on the opposite sides of the brain, had greater activity. Mirroring the Pro/Contra tendency, our experimental data showed that Anti-preferring neurons tended to also be Ipsi-preferring (Fig. 4b). But this tendency was not as strong as the Pro/Contra tendency (Fig. 4b). We, therefore, did not constrain the Anti pool to be either Contra-preferring or Ipsi-preferring. Our model had free parameters describing the sign and strength of connections between the units (Fig. 6a), the degree of silencing induced by optogenetic inactivation, the magnitude of additive noise at each timestep and others (Methods). Connections between the two sides of the SC are known to be both excitatory and inhibitory[18,36], so we did not specify connection signs.

We optimized model parameters by minimizing an error function defined such that low errors corresponded to a qualitative match to the control and the optogenetic inactivation results of Fig. 5d (Methods): namely, control trials had higher accuracy for Pro

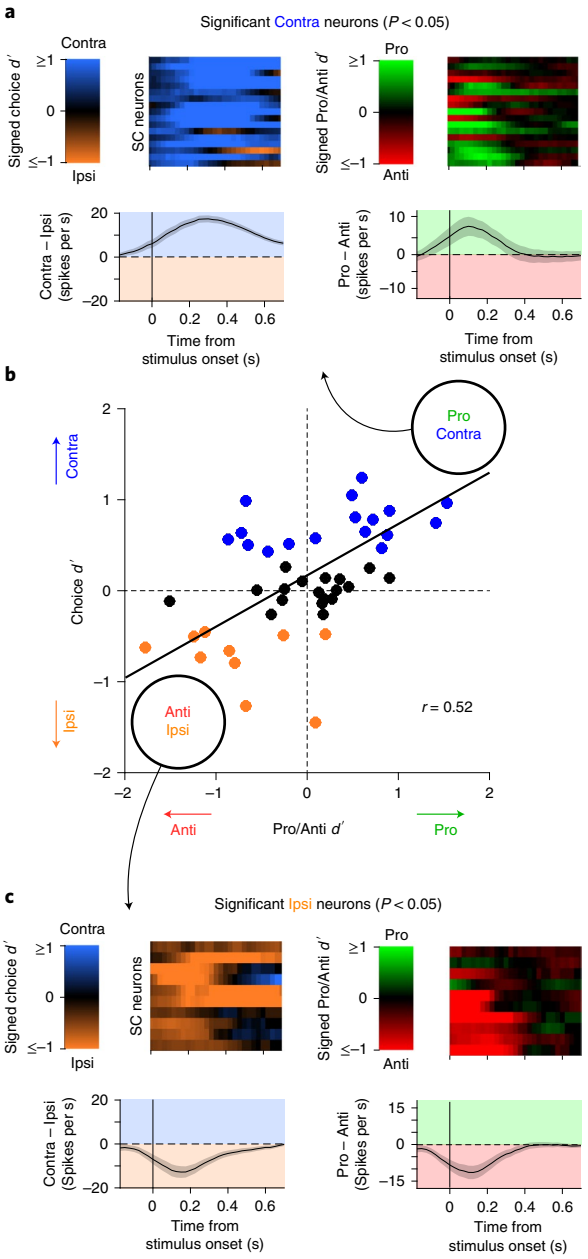

Fig. 4 | A relationship between task context and choice encoding around stimulus onset, suggesting two groups of SC delay/choice neurons. **a**, Neurons selected as having a significantly greater firing rate on trials when the animal oriented contralaterally to the recorded neuron ($n = 17$ neurons having $P < 0.05$, two-sided t-test, no adjustment for multiple comparisons). Left top: one neuron per row, with the color indicating the strength of Contra/Ipsi selectivity (d') as a function of time relative to the visual stimulus onset. Bin size = 250 ms, centered (that is, it includes spikes from ±125 ms relative to the plotted time point). Left bottom: mean ± s.e.m. firing rate difference (Contra − Ipsi) averaged over these neurons. Right: the same neurons as in the left panels analyzed for Pro/Anti selectivity and firing rate difference. Contra-preferring neurons tend to be Pro-preferring. Correct trials only. **b**, The signed Pro/Anti task context d' is plotted against the signed Contra/Ipsi choice d', both computed within the first time bin after stimulus appearance (0–250 ms). The two are significantly correlated (Pearson's correlation coefficient $r = 0.52$, $n = 45$, $P = 0.00025$, t-test), due to the prevalence of Pro/Contra and Anti/Ipsi units. **c**, As in **a** but showing significantly Ipsi-preferring neurons ($n = 10$). Ipsi-preferring neurons tend to be Anti-preferring.

compared to Anti (Extended Data Fig. 1c); delay period inactivation impaired accuracy on Anti trials but not Pro trials (Fig. 5d, middle); and choice period inactivation had no effect on choice accuracy in either Anti or Pro trials (Fig. 5d, right). We developed a 'frozen noise' approach to train the network to a specified % correct accuracy in each particular trial condition (Methods). After starting the minimizations of the error function from many thousands of different random parameter values, 373 of them had low final error; we refer to these as 'solutions' (Methods). When each solution was then tested with noise realizations different from those that they were trained on, the models replicated the inactivation patterns that we observed in experimental data (Fig. 6b,c). We found that model solutions that fit the delay and choice period inactivation data could also predict the full-trial and cue period inactivation data, with variability across solutions (Fig. 6d). To investigate whether the model dynamics encode similar information as those found in recorded SC neurons, we decoded Pro/Anti task context and Left/Right choice for each model solution (Methods). The average decoding patterns parallel those found in our electrophysiology data (Fig. 2): task context information during the task cue and delay period (Fig. 6e), followed by a strong choice signal after target stimulus presentation (Fig. 6f). Across individual model solutions, and similarly to the SC neural data of Fig. 4, we found both Anti/Ipsi-preferring and Anti/Contra-preferring units, with a prevalence of Anti/Ipsi preference (Extended Data Fig. 8a). To examine whether Anti/Ipsi and Anti/Contra units could also be found within individual models, we followed the same procedures with a more complex, six-node model in which each side of the brain had two Anti pools, each with its own dynamics and connectivity parameters (Extended Data Fig. 9a). Results with the six-node models matched the main results of the four-node models and contained, within individual model solutions, both Anti/Ipsi-preferring and Anti/Contra-preferring units, with a majority of Anti/Ipsi units (Extended Data Fig. 9d), as in the experimental data. More generally, the six-node results show that our conclusions can generalize beyond the four-node models. We conclude that choice formation circuitry lying purely within the SC and involving Pro/Contra and a majority Anti/Ipsi neurons is sufficient to reproduce our behavioral and optogenetic perturbation data.

We next asked whether the 373 solutions corresponded to variants of a single mechanism or many distinct dynamical mechanisms that solve the task. We used singular value decomposition (SVD) of the activity of the four model units across time to find a low-dimensional representation of all solutions in terms of their dynamics (Methods); the dynamics of each solution correspond to one point in this low-dimensional space (Fig. 7a). To our surprise, the dynamics across solutions were highly heterogeneous (Fig. 7a,b). The variability in dynamics is also reflected in variability in parameter values (Extended Data Fig. 10). Principal component analysis on the parameter values or dynamics revealed that more than ten principal components were required to explain 90% of the variance in parameter values or dynamics across the 373 solutions (Extended Data Fig. 8b), even though, within each individual solution, fewer than three dimensions were needed to explain variance across time in the trial (Extended Data Fig. 8c). These findings demonstrate that the simple dynamical circuit architecture of Fig. 6a can perform the task using a large variety of configurations.

Despite the highly varied dynamics and parameter values in different solutions, we identified two features that were tightly constrained and consistent across model solutions and one feature that previous literature had led us to expect to be tightly constrained but was not. First, almost all solutions had inhibitory connections from the Anti unit to the Pro unit on the same hemisphere (vertical weight from Anti to Pro unit, 365/373 negative, 97.9%; Fig. 7c and Extended Data Fig. 9c). This suggests that suppression of the 'default' Pro pathway by Anti task context representation, locally in the SC, might be important for avoiding reflexive Pro responses

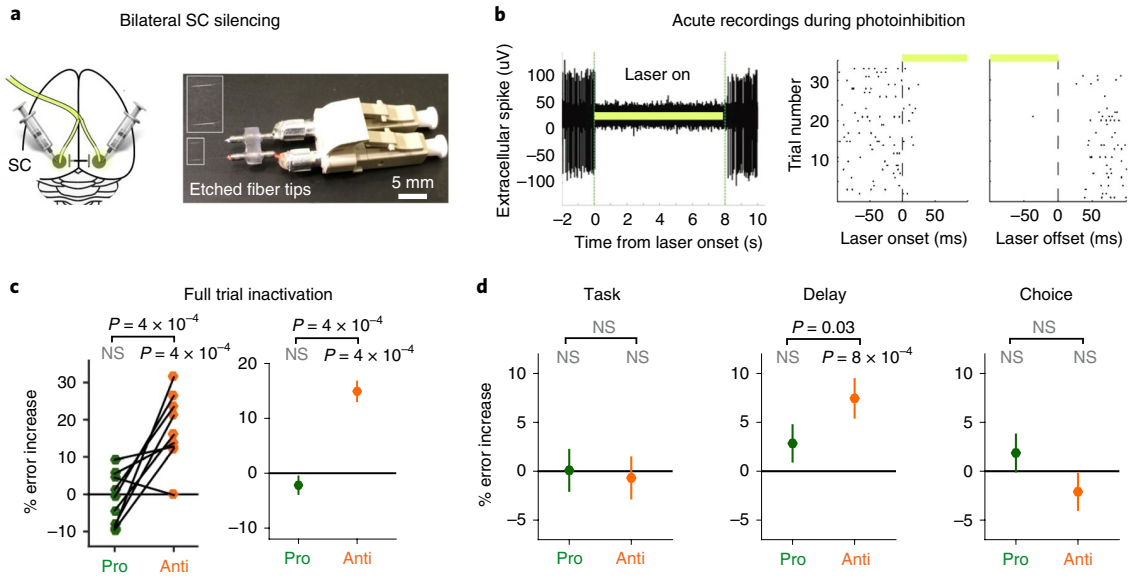

Fig. 5 | SC delay activity is required for the Anti task. a, Experimental design for bilateral SC optogenetic inactivation. Left: a schematic that indicates virus infection and laser stimulation in the SC on both hemispheres. Right: an example of the optical fiber implant. The taper of each fiber is chemically sharpened to be approximately 2 mm long for stronger and more unified light delivery. The distance between the two fibers is constructed to be exactly 3.6 mm to target bilateral SC. **b**, Physiological confirmation of optogenetic inactivation effect in an anesthetized animal. Left: acute extracellular recording of spontaneous activity in the SC expressing eNpHR3.0. Laser illumination period (8 s) is marked by the light green bar. Right: spike activity aligned to laser onset and laser offset over multiple trials. Note that the onset and offset of the inhibitory effect are on the scale of tens of milliseconds. **c**, Effect of full-trial inactivation of bilateral SC. Mean Pro (green) and Anti (orange) error rate increase due to SC inactivation for all individual rats ($n = 9$, left) and across all trials (Pro = 662 trials, Anti = 615 trials, right). Left: each data point represents the mean effect across sessions for a single rat. Right: means and s.e.m. across trials (concatenated across all 60 sessions). *P* values report two-sided bootstrap or permutation tests, shuffled 5,000 times. **d**, Effect of sub-trial inactivations of bilateral SC on Pro and Anti error rate (mean and s.e.m. across trials from 102 sessions). Statistical comparison between Pro and Anti effects were computed using a two-sided permutation test, shuffled 5,000 times. NS, not significant. Note that all types of inactivations were randomly interleaved for each session.

toward the target stimulus. Consistent with this modeling result, experimentally measured noise correlations between pairs of simultaneously recorded SC neurons encoding opposite task contexts were significantly negative (25 pairs, $P = 0.03$, two-sided *t*-test; Fig. 7d). Note that the connections from the Pro unit back to the ipsilateral Anti unit were not necessarily inhibitory (vertical weights from Pro to Anti unit, 67.6% negative; Extended Data Fig. 10), indicating an asymmetry in the circuit architecture of Pro and Anti representations that might parallel behavioral asymmetries. Second, most solutions had excitatory connections from the Anti unit to the Pro unit on the opposite hemisphere (diagonal weights from Anti to Pro unit, 339/373 positive, 90.9%; Fig. 7c and Extended Data Fig. 9c), constituting a pathway that executes the task-appropriate orienting response away from the target stimulus during Anti trials.

There was a small fraction of solutions that had positive vertical weights from the Anti to the ipsilateral Pro unit (dots to the right-hand side of vertical dashed line in Fig. 7c) or negative diagonal weights (dots below the horizontal dashed line in Fig. 7c), but most of these (34/38, 89.47%) had a more positive diagonal weight than the vertical weight (across all 373 solutions, 98.9% are above the dashed red diagonal line in Fig. 7c; also see Extended Data Fig. 9c), consistent with a functionally competitive inhibition mechanism between the two projections. A Schur decomposition analysis of the connectivity matrix showed that, compared to connectivity matrices that had the same symmetry constraints as our model (Fig. 6a), but were otherwise random, the weight matrices of the 373 solutions had over-represented positive eigenvalues on the activity modes representing the task context (differential activity of both Anti units compared to both Pro units, 94.9% of solutions) and diagonal activity patterns (Anti unit on one side co-activated with the Pro unit on the other, 98.4% of solutions; Extended Data Fig. 8d). Similar results were found in the six-node models (Extended Data Fig. 9e). The Schur decomposition analysis demonstrates that most solutions have stable task and diagonal activity patterns.

We expected to find mutual inhibition between nodes representing opposite decisions, which is a commonly proposed motif in the literature[8,37–39]. However, we found that model solutions did not require mutual inhibition between the Pro/Contra nodes (Fig. 7e and Extended Data Fig. 9b), even while displaying strong separation between the neural activity representing opposite decisions (see light versus dark green traces for the two Pro/Contra units in the examples of Fig. 7b).

In summary, by optimizing models of within-SC circuity to match behavioral and optogenetic results, we identified key anatomical and functional features of possible SC circuits for executive control. First, even in our simplified models with only four or six nodes, there are many very diverse circuits and dynamics that satisfy the experimental constraints. Second, in contrast to expectations from the literature[8,37–39], we found that direct mutual inhibition between nodes representing opposite decisions was not required and should not be taken as an experimental prediction. Third, two features that correspond to key processes of executive control—namely, (1) inhibiting task-inappropriate behavior and (2) executing task-appropriate actions—were found to be required, in the form of (1) inhibitory connections from Anti-preferring units to Pro-preferring units on the same hemisphere and (2) excitatory connections from Anti units to Pro units on the opposite hemisphere. These results support a role for the SC in executive control and delineate SC circuit properties to implement this role. We note that our data do not demonstrate that such a role would be exclusive

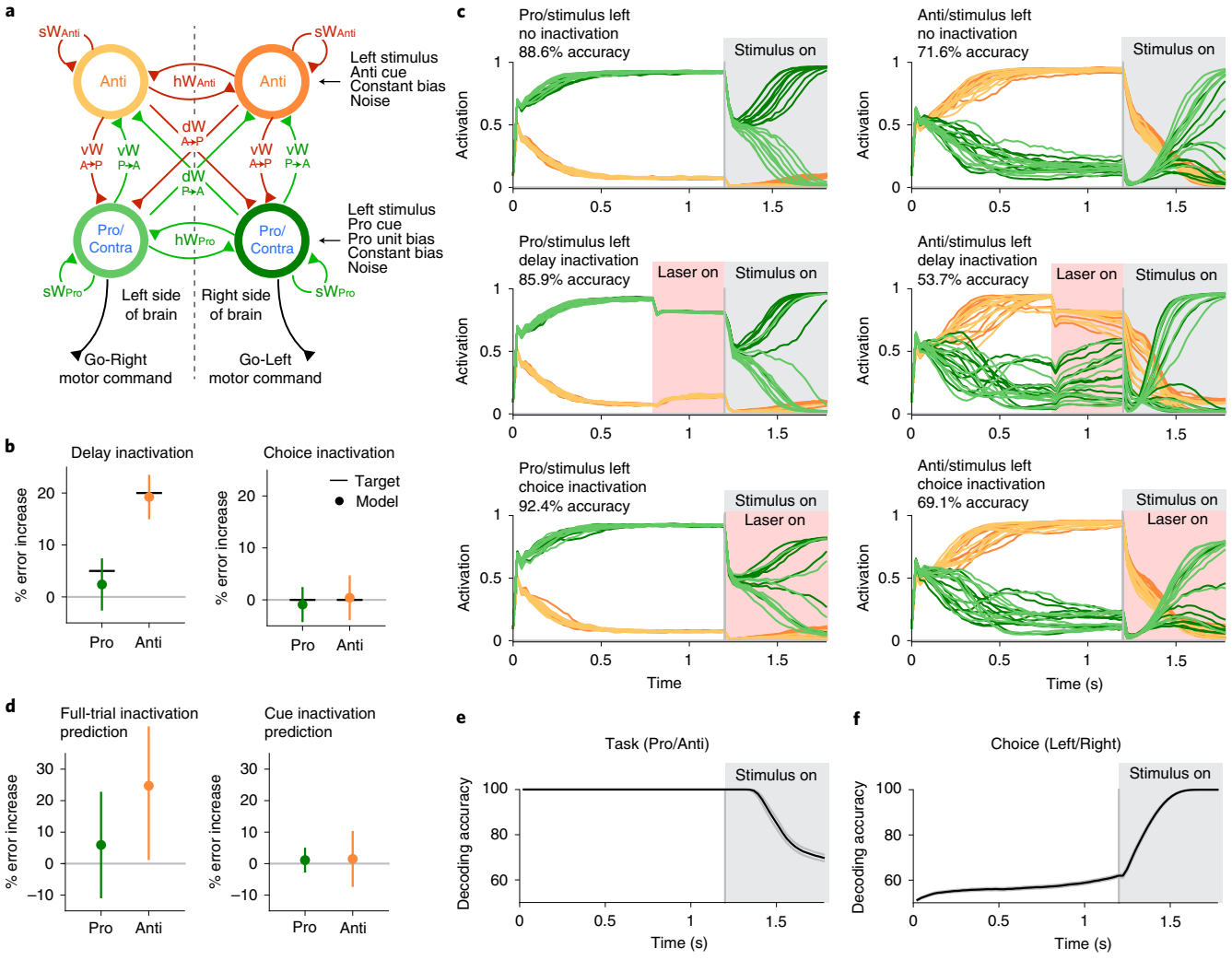

Fig. 6 | Dynamical SC model for flexible sensorimotor switching replicates optogenetic inactivation patterns. a, Schematic of SC model, showing four units, each representing a population of SC delay/choice neurons. Connection strengths are independent in each direction, as well as for Pro and Anti self-connections, for a total of eight connection parameters. Each unit also receives external inputs. **b**, Model fit to control, delay and choice period inactivation results. Target and model performance that qualitatively replicate the Pro (green) and Anti (orange) error rate changes after delay (left) and choice (right) period inactivations (mean ± 95% confidence intervals across all model solutions, $n = 373$ model solutions). **c**, For one example solution, activity of the four SC units (colors as in **a**) on ten example Pro (left) and Anti (right) trials in three different conditions: no inactivation (top row), delay period inactivation (middle row) and choice period inactivation (bottom row). Each trial had either 1.0-s or 1.2-s task cue and delay period, followed by a 0.45-s or 0.60-s choice period. Visual stimulus is presented on the left hemifield. Average accuracy on a test set of 10,000 trials is reported. Leftward-orienting responses correspond to trials where the dark green unit ends with higher activity than the light green unit; rightward-orienting choices correspond to the opposite ordering. We do not assume that optogenetic inactivation in the experiments is necessarily complete; consequently, inactivations in the model (middle and bottom rows) reduce, but do not completely silence, activity. **d**, Model prediction for full-trial inactivation (left) and task cue period inactivation (right), similar to **b**. **e**, Mean ± s.e.m. Pro/Anti task context decoding (Methods) across all model solutions as a function of time; correct and incorrect trials are included. **f**, Mean ± s.e.m. Left/Right choice decoding across all model solutions as a function of time; correct and incorrect trials are included.

to the SC; it might be performed in coordination with other executive control regions.

Discussion

We used sub-trial optogenetic perturbations, electrophysiological recordings and computational modeling of rat SC to investigate circuit mechanisms during executive control. Pro/Anti, the behavior that we used, has a cued task context ('Pro' versus 'Anti') that indicates whether the subjects should orient toward a visual stimulus (Pro task) or away from it (Anti task). Each trial of this behavior is composed of three successive phases (Fig. 1). First, the trial begins with presentation of a non-spatial context cue. Second, there is a brief delay period, during which the subjects should hold the identity of the current trial's context in memory. Third, the lateralized visual stimulus is presented, and subjects can begin to combine information about task context and the visual stimulus side, to form and express their left or right choice.

Electrophysiological recordings revealed that rat SC neuron firing rates encoded both task context (Pro versus Anti) and, after the lateralized visual stimulus, side choice. Across all recorded SC cells, we found neurons displaying all four possible Pro/Anti × Contra/Ipsi firing rate preferences (Fig. 1c–e and Extended Data Fig. 5a).

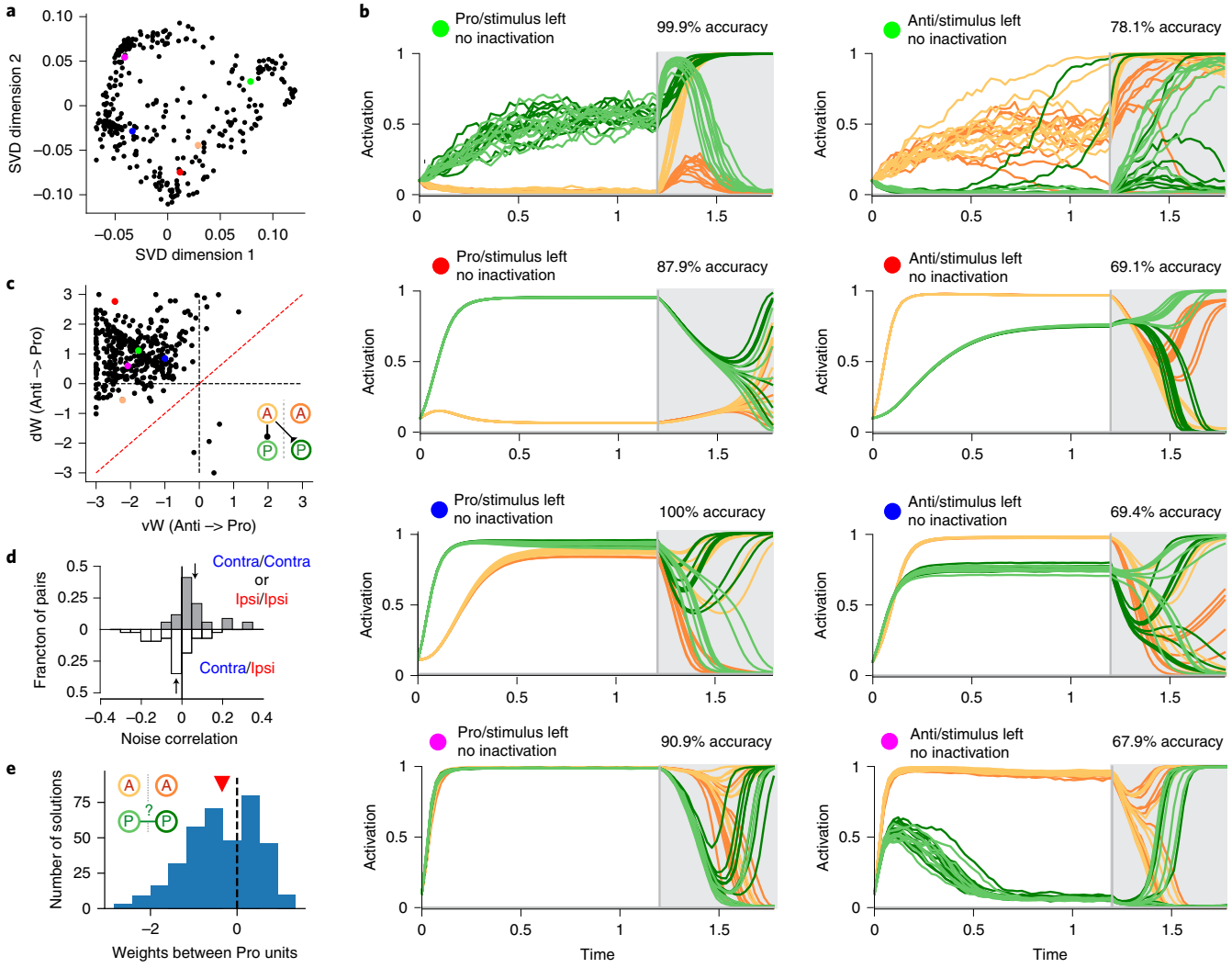

Fig. 7 | Common circuit mechanisms across heterogeneous model dynamics. a, Projection of model solutions onto the top two dimensions that maximally explain variance in model dynamics across solutions. Individual dots are unique model solutions. Colored dots refer to the example solutions shown in **b**; the orange dot is the example in Fig. 6c. **b**, Model unit activity on ten Pro and Anti trials from four example solutions, similar to Fig. 6c (control only). **c**, Scatter plot of diagonal weights (from Anti units to Pro units on the opposite hemisphere) against vertical weights (from Anti units to Pro units on the same hemisphere), for all model solutions. Equality line added for reference. Colored dots refer to example solutions shown in **b**. Inset cartoon summarizes mean connectivity patterns with inhibition from the Anti unit to the ipsilateral Pro unit and excitation to the contralateral Pro unit. **d**, Trial-by-trial noise correlation between pairs of simultaneously recorded neurons on one side of the SC, calculated for within-group pairs of neurons (Contra/Contra or Ipsi/Ipsi, upper histogram) and between-group pairs (Contra/Ipsi). Noise correlation distribution for within-group pairs was significantly shifted above 0 (mean = 0.082 ± 0.02; $P = 0.0003$, $n = 27$ pairs, two-sided t-test), whereas the between-group distribution was significantly shifted below 0 (mean = −0.052 ± 0.02; $P = 0.0306$, $n = 25$ pairs, two-sided t-test), consistent with negative vertical weights as predicted by the model. Arrows indicate the mean values. **e**, The distribution of horizontal weights between the two Pro units (as illustrated by the inset cartoon) for all model solutions. Red arrow marks the average value across solutions. The heterogeneity of this parameter suggests that mutual inhibition between nodes representing opposite choices was not a necessary feature for many solutions.

However, this apparent coding heterogeneity appeared more orderly in a subset of neurons. Within these neurons, referred to as 'delay/choice' neurons, there was a strong correlation between task context and choice selectivity where Pro-preference was more correlated with Contra-preference (Fig. 4 and Extended Data Fig. 5b). This result reveals critical structure in neural representations of the task and provides an important constraint for circuit models of the phenomenon.

We also compared SC recordings to recordings from medial PFC and the FOF—two rodent cortical regions that are primary candidates for forming choices during Pro/Anti behavior. Remarkably, we found that delay/choice SC neurons encoded the side choice much faster, by ~200 ms, than either medial PFC or FOF neurons (Figs. 2c and 3c). This contrasts with previous findings, using a perceptual decision task in mice that did not require executive control, of similar choice decoding timing in frontal cortex and midbrain neurons[40]. The long timing difference between SC and FOF or PFC is sufficient for information to reverberate back and forth across the brain. Such a long duration suggests that, at least in this rat behavior, the SC leads choice formation. PFC or other brain structures might still play an instrumental role in enabling SC dynamics to reach the correct choice, and we cannot rule out that an as-yet unrecorded region could show even earlier decision signals. But our current data place SC as a leading candidate for playing a central, driving role in choice computation.

We note that the SC is a highly conserved structure of the vertebrate brain, whereas the PFC has undergone dramatic changes during evolution[41,42], which means that the relative roles of SC and PFC in executive control might be quite different across rodents and primates. Our behavior closely parallels analogous primate paradigms to facilitate such cross-species comparison. Single-neuron recordings in monkey SC[27] and dorsolateral PFC[43,44] have revealed heterogeneous task-relevant signals similar to those observed here (Fig. 1c–e), but a direct comparison of monkey cortical and SC population decoding accuracy and latency remains to be done.

The causal contribution of SC activity to spatial decision-making, target selection, spatial attention and avoidance/approach behavior has most often been investigated using unilateral perturbations[10,25,45–47]. These experiments, all within the spatial domain, have established the SC's importance in contralateral control of orienting responses. Consistent with those findings, unilateral pharmacological SC inactivation during our Pro/Anti task also results in a contralateral impairment[3].

In this study, however, we used bilateral optogenetic perturbations (Fig. 5). Notably, the optogenetic inactivation experiments provide much more specific and revealing information than the hours-long pharmacological inactivations that we used previously[3]. The lack of effect of SC inactivation during the sensory cue suggests that cue period encoding in the SC is not required for behavior; other regions might provide redundant information during the cue period. On the other hand, when the sensory cue for task context is no longer present, and before a lateralized choice can be formed, context encoding in the SC is causally required for Anti behavior (Fig. 5d, middle versus left panel). Although we did not specifically target medial or lateral SC in our recording and inactivation experiments, the selective requirement of SC activity for Anti responses is reminiscent of previous studies that implicate the medial SC in avoidance behavior[48]. It should be noted that, although our optogenetic inactivation should be restricted to SC neurons, selective upstream inputs to the SC could potentially be affected[49].

In contrast to the behavioral impairment caused by delay period inactivation, optogenetic inactivations of the SC during the immediately subsequent period, corresponding to when choices can be formed and expressed, did not impair choices (Fig. 5d, right). The amount of time for visual information to reach the superficial (~35 ms)[50] and then deep layers of the SC is considerably longer than the optogenetic onset time (~10 ms) (Fig. 5b). It is, thus, unlikely that choices could be formed before the optogenetic effects. One caveat is that we quantified the temporal precision of optogenetic inactivation of SC activity in anesthetized rats (Methods). The time course of inactivation in awake animals might be different.

Given that the electrophysiological data suggest that the SC plays a leading role in choice formation, the lack of an inactivation effect during the choice formation period seems, at first, surprising. However, because optogenetic inactivation does not produce 100% silencing, the choice period result does not necessarily preclude the SC from playing a central role in choice formation. The result does, however, indicate that SC dynamics during the choice period should be substantially more robust to perturbation than during the context encoding period. Although reminiscent of the lack of response period perturbation effects reported in a previous delayed orienting task[25], we think that the underlying cause is very different. In Kopec et al.[25], animals could form a spatial action plan much earlier than the response period. The lack of an impairment from response period inactivation was interpreted as due to the inactivation occurring after spatial action planning. In contrast, in the Pro/Anti task, spatial action planning cannot be formed before the inactivated choice period, because that is the critical window of sensorimotor transformation when task cue and direction information are first combined to guide action. Susceptibility to perturbation during the delay period, but robustness during the choice period, appears to be not trivial to replicate in circuit models of the SC.

To systematically probe whether one could, in fact, construct SC circuit models in which the SC computed choice in a manner susceptible to delay period inactivation but robust to choice period inactivation, we built a simplified recurrent network model of the SC. Common practice in the field would be to find a point in the model parameter space that satisfies the experimental data constraints[8,37]. We call such a point a 'circuit solution.' Given the disparate constraints posed by our data, would any circuit solutions exist? Large-scale computational searches for solutions revealed that, indeed, they exist (Fig. 6). Moreover, there exist many solutions, and they are quite diverse in nature (Fig. 7). How should we think about circuit hypotheses if there are many circuit solutions compatible with the data? We reasoned that features common across solutions would be predictions of our modeling framework as a whole, not just of an individual specific hypothesis, and we should, thus, identify common features as particularly important model predictions. Past model circuits built to perform the Pro/Anti behavior (and not constrained or informed by our SC data) have features corresponding to response inhibition and to vector inversion, as well as mutual inhibition between nodes representing opposite contexts and opposite choices[8,38]. We found that motifs corresponding to response inhibition and to vector inversion were, indeed, common across our diverse set of SC solutions. However, even though response inhibition (that is, inhibition from Anti units to Pro units) was necessary, we found that reciprocal mutual inhibition back from the Pro units to the Anti units was not necessary. Most surprisingly, we found that an almost universal feature of circuit models built to decide between possible options—namely, mutual inhibition between nodes representing opposite choices[8,37–39]—was not necessary (Fig. 7e). Our results, thus, suggest that common assumptions regarding decision-making circuitry must be taken with care. Future work is needed to investigate whether the dynamical modes identified in our models can be generalized to other model architectures and whether detailed response patterns, such as increases or decreases in firing rates, are important for model performance.

To summarize, our data and modeling show how SC circuits in the Pro/Anti behavior represent context information and combine it with sensory information to compute choice. A key finding is the physiological identification of a subset of SC neurons that link context and choice representation in a systematic way. These SC neurons appear to be important for choice computation during the Pro/Anti behavior. Populations of models of the neural circuit dynamics between these neurons, built to match our experimental data, single out key circuit mechanisms in the form of specific connectivity predictions that are robust across highly diverse model solutions. Our data support participation of the SC in all periods of the Pro/Anti behavior, as well as a leading role for the SC in choice computation, and our circuit models set out a predictive framework with which to further elucidate these processes.

Online content

Any methods, additional references, Nature Research reporting summaries, source data, extended data, supplementary information, acknowledgements, peer review information; details of author contributions and competing interests; and statements of data and code availability are available at https://doi.org/10.1038/s41593-021-00865-x.

Received: 2 October 2019; Accepted: 4 May 2021;
Published online: 3 June 2021

References

1. Miller, E. K. & Cohen, J. D. An integrative theory of prefrontal cortex function. *Annu. Rev. Neurosci.* **24**, 167–202 (2001).

2. Hallett, P. E. Primary and secondary saccades to goals defined by instructions. *Vis. Res.* **18**, 1279–1296 (1978).
3. Duan, C. A., Erlich, J. C. & Brody, C. D. Requirement of prefrontal and midbrain regions for rapid executive control of behavior in the rat. *Neuron* **86**, 1491–1503 (2015).
4. Weiler, J. & Heath, M. Task-switching in oculomotor control: unidirectional switch-cost when alternating between pro- and antisaccades. *Neurosci. Lett.* **530**, 150–154 (2012).
5. Munoz, D. P. & Everling, S. Look away: the anti-saccade task and the voluntary control of eye movement. *Nat. Rev. Neurosci.* **5**, 218–228 (2004).
6. Everling, S. & Fischer, B. The antisaccade: a review of basic research and clinical studies. *Neuropsychologia* **36**, 885–899 (1998).
7. Hutton, S. B. & Ettinger, U. The antisaccade task as a research tool in psychopathology: a critical review. *Psychophysiology* **43**, 302–313 (2006).
8. Lo, C.-C. & Wang, X.-J. Conflict resolution as near-threshold decision-making: a spiking neural circuit model with two-stage competition for antisaccadic task. *PLoS Comput. Biol.* **12**, e1005081 (2016).
9. Everling, S. & Johnston, K. Control of the superior colliculus by the lateral prefrontal cortex. *Philos. Trans. R. Soc. Lond. B Biol. Sci.* **368**, 20130068 (2013).
10. Felsen, G. & Mainen, Z. F. Neural substrates of sensory-guided locomotor decisions in the rat superior colliculus. *Neuron* **60**, 137–148 (2008).
11. Sparks, D. L. & Hartwich-Young, R. The deep layers of the superior colliculus. *Rev. Oculomot. Res.* **2**, 213–255 (1989).
12. Wurtz, R. H. & Goldberg, M. E. Activity of superior colliculus in behaving monkey. 3. Cells discharging before eye movements. *J. Neurophysiol.* **35**, 575–586 (1972).
13. Evans, D. A., Stempel, A. V., Vale, R. & Branco, T. Cognitive control of escape behaviour. *Trends Cogn. Sci.* **23**, 334–348 (2019).
14. Gandhi, N. J. & Katnani, H. A. Motor functions of the superior colliculus. *Annu. Rev. Neurosci.* **34**, 205–231 (2011).
15. Robinson, D. A. Eye movements evoked by collicular stimulation in the alert monkey. *Vis. Res.* **12**, 1795–1808 (1972).
16. Johnston, K., Koval, M. J., Lomber, S. G. & Everling, S. Macaque dorsolateral prefrontal cortex does not suppress saccade-related activity in the superior colliculus. *Cereb. Cortex* **24**, 1373–1388 (2014).
17. Basso, M. A. & May, P. J. Circuits for action and cognition: a view from the superior colliculus. *Annu Rev. Vis. Sci.* **3**, 197–226 (2017).
18. Wolf, A. B. et al. An integrative role for the superior colliculus in selecting targets for movements. *J. Neurophysiol.* **114**, 2118–2131 (2015).
19. Krauzlis, R. J., Lovejoy, L. P. & Zénon, A. Superior colliculus and visual spatial attention. *Annu. Rev. Neurosci.* **36**, 165–182 (2013).
20. Crapse, T. B., Lau, H. & Basso, M. A. A role for the superior colliculus in decision criteria. *Neuron* **97**, 181–194.e6 (2018).
21. Horwitz, G. D., Batista, A. P. & Newsome, W. T. Representation of an abstract perceptual decision in macaque superior colliculus. *J. Neurophysiol.* **91**, 2281–2296 (2004).
22. Duan, C. A. et al. A cortico-collicular pathway for motor planning in a memory-dependent perceptual decision task. *Nat. Commun.* **12**, 2727 (2021).
23. Schmitt, L. I. et al. Thalamic amplification of cortical connectivity sustains attentional control. *Nature* **545**, 219–223 (2017).
24. Erlich, J. C., Bialek, M. & Brody, C. D. A cortical substrate for memory-guided orienting in the rat. *Neuron* **72**, 330–343 (2011).
25. Kopec, C. D., Erlich, J. C., Brunton, B. W., Deisseroth, K. & Brody, C. D. Cortical and subcortical contributions to short-term memory for orienting movements. *Neuron* **88**, 367–377 (2015).
26. Felsen, G. & Mainen, Z. F. Midbrain contributions to sensorimotor decision making. *J. Neurophysiol.* **108**, 135–147 (2012).
27. Everling, S., Dorris, M. C., Klein, R. M. & Munoz, D. P. Role of primate superior colliculus in preparation and execution of anti-saccades and pro-saccades. *J. Neurosci.* **19**, 2740–2754 (1999).
28. Rigotti, M. et al. The importance of mixed selectivity in complex cognitive tasks. *Nature* **497**, 585–590 (2013).
29. Mante, V., Sussillo, D., Shenoy, K. V. & Newsome, W. T. Context-dependent computation by recurrent dynamics in prefrontal cortex. *Nature* **503**, 78–84 (2013).
30. Pagan, M., Urban, L. S., Wohl, M. P. & Rust, N. C. Signals in inferotemporal and perirhinal cortex suggest an untangling of visual target information. *Nat. Neurosci.* **16**, 1132–1139 (2013).
31. Hanks, T. D. et al. Distinct relationships of parietal and prefrontal cortices to evidence accumulation. *Nature* **520**, 220–223 (2015).
32. Prinz, A. A., Bucher, D. & Marder, E. Similar network activity from disparate circuit parameters. *Nat. Neurosci.* **7**, 1345–1352 (2004).
33. Fisher, D., Olasagasti, I., Tank, D. W., Aksay, E. R. F. & Goldman, M. S. A modeling framework for deriving the structural and functional architecture of a short-term memory microcircuit. *Neuron* **79**, 987–1000 (2013).
34. Bittner, S. R. et al. Interrogating theoretical models of neural computation with deep inference. Preprint at *bioRxiv* https://doi.org/10.1101/837567 (2019).
35. Dean, P., Mitchell, I. J. & Redgrave, P. Contralateral head movements produced by microinjection of glutamate into superior colliculus of rats: evidence for mediation by multiple output pathways. *Neuroscience* **24**, 491–500 (1988).
36. May, P. J. The mammalian superior colliculus: laminar structure and connections. *Prog. Brain Res.* **151**, 321–378 (2006).
37. Machens, C. K., Romo, R. & Brody, C. D. Flexible control of mutual inhibition: a neural model of two-interval discrimination. *Science* **307**, 1121–1124 (2005).
38. Cutsuridis, V., Smyrnis, N., Evdokimidis, I. & Perantonis, S. A neural model of decision-making by the superior colliculus in an antisaccade task. *Neural Netw.* **20**, 690–704 (2007).
39. Wong, K.-F. & Wang, X.-J. A recurrent network mechanism of time integration in perceptual decisions. *J. Neurosci.* **26**, 1314–1328 (2006).
40. Steinmetz, N. A., Zatka-Haas, P., Carandini, M. & Harris, K. D. Distributed coding of choice, action and engagement across the mouse brain. *Nature* **576**, 266–273 (2019).
41. Uylings, H. B. M., Groenewegen, H. J. & Kolb, B. Do rats have a prefrontal cortex? *Behav. Brain Res.* **146**, 3–17 (2003).
42. Seamans, J. K., Lapish, C. C. & Durstewitz, D. Comparing the prefrontal cortex of rats and primates: insights from electrophysiology. *Neurotox. Res.* **14**, 249–262 (2008).
43. Everling, S. & DeSouza, J. F. X. Rule-dependent activity for prosaccades and antisaccades in the primate prefrontal cortex. *J. Cogn. Neurosci.* **17**, 1483–1496 (2005).
44. Johnston, K. & Everling, S. Monkey dorsolateral prefrontal cortex sends task-selective signals directly to the superior colliculus. *J. Neurosci.* **26**, 12471–12478 (2006).
45. Zénon, A. & Krauzlis, R. J. Attention deficits without cortical neuronal deficits. *Nature* **489**, 434–437 (2012).
46. McPeek, R. M. & Keller, E. L. Deficits in saccade target selection after inactivation of superior colliculus. *Nat. Neurosci.* **7**, 757–763 (2004).
47. Sahibzada, N., Dean, P. & Redgrave, P. Movements resembling orientation or avoidance elicited by electrical stimulation of the superior colliculus in rats. *J. Neurosci.* **6**, 723–733 (1986).
48. Dean, P., Redgrave, P. & Westby, G. W. Event or emergency? Two response systems in the mammalian superior colliculus. *Trends Neurosci.* **12**, 137–147 (1989).
49. Aschauer, D. F., Kreuz, S. & Rumpel, S. Analysis of transduction efficiency, tropism and axonal transport of AAV serotypes 1, 2, 5, 6, 8 and 9 in the mouse brain. *PLoS ONE* **8**, e76310 (2013).
50. Franceschi, G. & Solomon, S. G. Visual response properties of neurons in the superficial layers of the superior colliculus of awake mouse. *J. Physiol.* **596**, 6307–6332 (2018).

Methods

Subjects. Twenty-four adult male Long–Evans rats (Taconic) were used for the experiments presented in this study. Of these, 12 rats were used for electrophysiology recordings, and 12 rats were implanted with optical fibers for the optogenetic inactivation and yellow fluorescent protein (YFP) control experiments. Animal use procedures were approved by the Princeton University Institutional Animal Care and Use Committee and carried out in accordance with National Institutes of Health standards. Rats used in the experimental and control groups were randomly chosen from a common pool of purchased animals.

Behavior. Rats were trained on the Pro/Anti task-switching behavior[3]. Each trial began with an LED turning on in the center port, instructing the rats to nose-poke there to initiate a trial. They were required to keep their noses in the center port until the center LED offset (nose fixation). Broken fixation trials were ignored in all analyses. During the first 1 s of nose fixation, a Pro or Anti sound was played (clearly distinguishable FM-modulated sounds) to indicate the current task, followed by a 500-ms silent delay when rats had to remember the current task while maintaining nose fixation. The center LED was then turned off, allowing the animal to withdraw from the center port. The withdrawal would trigger either a left or right LED to turn on as the target stimulus, which remained on until rats poked into one of the side ports. Trials with left or right LED were randomly interleaved throughout each session. RT is defined as the time from target onset until side poke. On a Pro trial, rats were rewarded for orienting toward the side LED; on an Anti trial, rats were rewarded for orienting away from the side LED and into the port without light. A correct choice was rewarded by 24 µl of water; an incorrect choice resulted in a loud sound, no reward and a short timeout. To ensure that all sub-trial optogenetic inactivation conditions have the same duration for laser stimulation (750 ms), all rats implanted with optical fibers were trained on a modified version of the behavior where the task cue period and the delay period both lasted 750 ms instead of the 1-s cue period and the 500-ms delay period as in the original design.

In all recording and inactivation sessions, rats performed alternating blocks of Pro and Anti trials, where block switches occurred within single sessions, after a minimum of 15 trials per block, and when a local estimate of performance (over the last ten trials in this block) reached a threshold of 70% correct. Detailed training procedures and codes can be found in a previous report[3]. All data collection and analysis were not performed blinded to the conditions of the experiments.

Recordings. Rats were implanted with custom-made movable microdrives, and recordings were made with platinum–iridium tetrodes[24]. To target the prelimbic (PL) area of PFC (+3.2 anteroposterior (AP) mm, ±0.75 mediolateral (ML) mm from bregma), tetrodes were initially positioned at ~1.5 mm below brain surface and were advanced daily during recording sessions to sample different neurons. To target the intermediate and deep layers of the SC (−6.8 AP mm, ±1.8 ML mm), tetrodes were initially positioned at ~3 mm below brain surface and advanced daily. Electrode placements were confirmed with histology. Four rats had both PL and SC implants (same hemisphere); two rats had a PL implant only; and one rat had an SC implant only. Five rats had FOF implants, with coordinates similar to those used in ref. [24]. The choice of recording area and hemisphere side was assigned randomly for each rat.

Analysis of animals' head orientation angles during recording. To examine if animals used any overt embodied strategy to encode the Pro/Anti task context during the delay period, we analyzed animals' head orientation angles in 21 SC recording sessions with reliable head tracking (defined as sessions with >25 correct Pro trials and >25 correct Anti trials with low variance of head angles within trials—that is, within-trial s.d. of head orientations <10°). Video tracking of rats' head orientation was acquired using red and blue LEDs placed on the tetrode recording drive head stages of the implanted rats (Neuralynx), as previously described[24]. For each trial in each session, normalized continuous head angle data were binned for each 5-ms time bin during the fixation period. Receiver operating characterisitc (ROC) analysis was conducted to discriminate head angles on Pro versus Anti trials for each time bin. Significant area under the curve (AUC) values ($P < 0.01$) are shown for all sessions and all time points. Non-significant AUC values were set to 0.5.

Analysis of neural data. Spike sorting was done manually using SpikeSort3D (Neuralynx), and only isolated single units were included in the following analyses. To perform analyses on the neural population, we only analyzed neurons recorded for a sufficient number of trials. More specifically, we only analyzed neurons for which we had collected responses during at least 25 correct trials for each of the four possible task conditions (Pro-Go-Right, Pro-Go-Left, Anti- Go-Right and Anti-Go-Left). This resulted in the analysis of 193 neurons (out of 215) in SC, and 291 neurons (out of 331) in PFC. Unless otherwise noted, all analyses were performed on correct trials. The response of each neuron was quantified by counting the number of spikes in 250-ms-wide bins. In all analyses (except in Supplementary Figs. 2 and 4), the response was aligned to the time when the target stimulus appeared (that is, the time of withdrawal from the center port). The temporal gap between the fixation offset (center LED turning off) and target stimulus onset (upon the animal's withdrawal from the center poke) was controlled by animals and, thus, variable on each trial. On average, rats withdrew from the center port 127 ms after fixation offset. Therefore, in all figures, we indicate the start of the delay period (end of task cue presentation) 0.627 s before target stimulus onset (500-ms delay + 127 ms) and the start of task cue presentation at 1.627 s before target onset (1 s of task cue presentation before the delay). To examine SC's role in the execution of motor responses, in Supplementary Fig. 4 we aligned SC neural activity to the time of side-poke. Unless otherwise noted, in all figures except Fig. 4, the analysis is causal—that is, the value plotted at time 0 refers to the neural activity in a time bin between −250 ms and 0 ms.

Quantification of single-neuron selectivity. The amount of information encoded by a single neuron about a task variable was measured at each time point using d', defined as the difference in the number of spikes fired in response to two generic task conditions (here named A and B), normalized by the square root of the pooled variance: $d' = \frac{\mu A - \mu B}{\sqrt{\frac{\sigma^2 A + \sigma^2 B}{2}}}$, where μ_A indicates the mean spike count in response to condition A, μ_B indicates the mean spike count in response to condition B, σ_A^2 indicates the variance across trials of the spike count in response to condition A and σ_B^2 indicates the variance across trials of the spike count in response to condition B.

Information about the task context (Pro/Anti d') was computed by comparing the responses during Pro trials and the responses during Anti trials (with positive d' indicating Pro preference). Information about the rat's choice (choice d') was computed by comparing the responses during trials that resulted in an orienting movement contralateral to the recorded neuron and trials that resulted in an ipsilateral orienting movement (with positive d' indicating Contra preference) (Fig. 1c–e). Quantification by computing the area under the ROC curves or firing rate differences led to similar results (Supplementary Fig. 3).

The threshold above which a single d' value was considered significantly different than 0 was computed based on the pairwise t-test between the two conditions, using a P value of 0.05. When we evaluated the significance of d' values computed at multiple time points (Fig. 3a), a shuffling procedure was also employed to correct for multiple comparisons. In this procedure, the d' at each time point was recomputed 100 times after randomly shuffling the labels of Pro and Anti trials, and the 95th percentile of the resulting overall distribution of shuffled d' values was used as the significance threshold.

Single-neuron selectivity about the task context was used to define two distinct classes of neurons (Fig. 3a). 'Cue neurons' were defined as those with peak Pro/Anti d' at a time while the task cue was still being presented. Delay/choice neurons were defined as those with peak Pro/Anti d' at times after the task cue was no longer present. Neurons whose Pro/Anti d' was never significantly different from 0 were excluded from both groups.

Within the class of 'delay/choice neurons', we used single-neuron selectivity about the choice in the first time bin after stimulus presentation (that is, from 0 to 250 ms) to further subdivide these cells into two groups (Fig. 4). 'Contra neurons' had a significantly higher response on trials with contralateral-orienting choices, whereas 'Ipsi neurons' had a significantly higher response on trials with ipsilateral choices.

Population-level decoding analysis. To determine the amount of task-relevant information available in the SC and PFC neural populations at each time point, we performed a series of cross-validated linear classification analyses[30]. For each analysis, we considered the spike count responses of a population of N neurons to a task condition as a population 'response vector' $\mathbf{x}$, and we randomly assigned 60% of the recorded trials (30 trials) as the training set and the remaining 40% of the trials (20 trials) as the test set. The training set was used to compute the linear hyperplane that would optimally separate the population response vectors corresponding to two different task conditions (for example, Pro trials versus Anti trials). This linear readout can also be written as $f(x) = \mathbf{w}^T\mathbf{x} + b$ where $\mathbf{w}$ is the n-dimensional vector of weights applied to each of the neurons, and b is a scalar threshold. The classification of a test response vector $\mathbf{x}$ was then assigned depending on the sign of $f(x)$, and the performance was computed as the fraction of correct classifications over 500 resampling iterations. Because some of the neurons were recorded in different sessions, trials were always shuffled on each iteration to destroy any artificial trial-by-trial correlations. The hyperplane and threshold were computed using a support vector machine algorithm using the LIBSVM library (https://www.csie.ntu.edu.tw/~cjlin/libsvm).

When comparing the classification performances for neural populations with different numbers of neurons, we randomly subsampled identical numbers of neurons without replacement on each iteration. Because the overall average firing rate was higher in SC than in PFC, we tested whether matching firing rates was sufficient to explain the classification result (Supplementary Fig. 8a), by removing single spikes at random from the SC dataset until the average firing rates were matched and by performing, again, the classification analysis on the equalized SC population.

When classification analyses were used to compare performances during correct and error trials (Fig. 3b), we always trained the classifier using correct trials, and we tested the classifier using either correct or error trials. The number

of trials used for testing was limited by the neuron with the fewest number of error trials per condition (nine trials).

To compute the latency of the rise in choice classification performance for different neural populations (Figs. 2c and 3c), we followed a previously reported method[51]. We evaluated the average time after the appearance of the target stimulus necessary for the population readout to reach a fixed threshold. More specifically, on each iteration of the resampling procedure we computed the classification performances for each time point, we smoothed the resulting curve by averaging the value with its five immediately previous time points (that is, a causal filter), and we noted the time point where the curve crossed the performance threshold. We computed the mean and the standard error of the latency as the mean and standard deviation of these values. For each number of neurons being used ($n = 193$ in Fig. 2c and $n = 29$ in Fig. 3c), the threshold was chosen so that curves from individual resamples would be unlikely to reach it by chance, yet all of the resamples would reach it at some point in time. Consequently, a performance threshold of 0.7 was used for Fig. 2c, and 0.65 was used for Fig. 3c. When comparing latencies across two populations, we computed the P value using a non-parametric permutation test, where we determined the fraction of resampling iterations for which the latency difference was flipped in sign relative to the actual difference between the means of the full dataset[51]. We further tested how these measurements of latency in the rise of classification performance depended on the total number of neurons (Supplementary Fig. 8b and Supplementary Information).

To further illustrate the early onset of choice information in the SC population compared to other cortical populations (Fig. 2c), we also compared neurons recorded from a different frontal cortical area, the FOF. We recorded 429 single units in the FOF in a version of the Pro/Anti task with a shorter delay period. All timings after stimulus onset are the same for SC, PFC and FOF recordings, thus providing a fair comparison for the onset of choice information in these populations. As described previously, when comparing the classification performances for neural populations with different numbers of neurons, we randomly subsampled identical numbers of neurons without replacement on each iteration ($n = 193$ neurons).

To compute the significance of differences in the magnitude (or latency) of population performances, we adopted a bootstrap approach based on our resampling procedure[52]. More specifically, we first evaluated the average performance (or latency) across all iterations for the two populations, and we then computed the P value as the fraction of iterations in which, by chance, the value for the population with the lower average was above the value for the population with the higher average.

Optical fiber construction, virus injection and fiber implantation. Chemically sharpened optical fibers (50/125 µm LC–LC duplex fiber cable, http://www.fibercables.com) were prepared as previously described[31]. To ensure that the distance between the two optical fibers was the distance between bilateral SC (3.6 mm), we inserted two metal cannulae into a plastic template and guided the optical fibers through the cannulae, which were 3.6 mm apart (Fig. 5a).

Basic virus injection techniques were identical to those described previously[31]. At the targeted coordinates (SC, −6.8 AP mm, ±1.8 ML mm from bregma), two injections of 9.2 nl of adeno-associated virus (AAV) (AAV5-CaMKIIα-eYFP-eNpHR3.0 for inactivations, nine rats; AAV5-CaMKIIα-eYFP for controls, three rats) were made every 100 µm in depth starting 3.5 mm below brain surface for 1.5 mm. Four additional injection tracts were completed: one 500 µm anterior, one 500 µm posterior, one 500 µm medial and one 500 µm lateral from the central tract. A total of 1.5 µl of virus was injected over the course of 30 min. Chemically sharpened bilateral SC fiber implant was lowered down the central injection track, with the tip of each fiber positioned at 4.4 mm below brain surface to target the center of SC's intermediate and deep layers. Training was resumed 5 days after surgery. Virus expression was allowed to develop for 8 weeks before behavioral testing began.

Optogenetic inactivation and analysis. For each inactivation session, animals' implants were connected to a 1-m patch cable connected to a fiber rotary joint (Princetel) mounted above the behavioral chamber. A 200-mW, 532-nm laser (OEM Laser Systems) was then connected to deliver constant light at 25 mW per site, with a <5 mW difference between the left and right SC. Laser illumination occurred on 25% randomly chosen trials in each behavioral session. Different optogenetic conditions (3-s full-trial inactivation, 750-ms task cue, 750-ms delay or 750-ms choice period inactivation) were randomly interleaved for all sessions to control for behavioral fluctuations across days. Choice period inactivation started at the onset of visual target and lasted 750 ms, covering the time it took animals to form and execute the orienting choice into the side-poke (690.8 ± 39.1 ms, mean ± s.e.m. across animals' median RT in optogenetic inactivation sessions). Switch trials were excluded in these analyses.

Behavioral changes due to optogenetic inactivation were quantified as the performance difference between inactivation (laser) trials and control (no-laser) trials from the same sessions. These results are then compared to YFP control data. For each session, we calculated the baseline error rate or RT for Pro and Anti control trials and subtracted that mean value from the performance on individual inactivation trials. After obtaining the normalized changes in performance due to inactivation for individual sessions, we concatenated trials across all sessions and all rats and computed the mean and s.e.m. across trials. Non-parametric bootstrap procedures or permutation tests were used to compute significance values (shuffled 5,000 times). All rats were included in the full-trial inactivation analyses. For sub-trial inactivation analyses, we only included the rats (8/9) that had significant full-trial effects.

Acute characterization of optogenetic effects. To measure the effects of optogenetic inactivation on neural activity, acute recordings of infected SC neurons were performed in anesthetized rats (Fig. 5b). An etched fiber optic and sharp tungsten electrode (0.5 or 1.0 MΩ) were independently advanced to the center of the infected area. For each neuron tested, baseline neural activity was recorded for 2 s, followed by 8 s of laser stimulation at 25 mW, and another 2 s of post-stimulation recording, repeated for >10 times. We observed that the onset and offset of optogenetic inactivation of neural activity was within 50 ms of laser onset and offset (Fig. 5b).

Model setup. Our model consists of four dynamical units; each unit had an external (V_i) and an internal (U_i) variable. The relationship between the internal and external variables is given by:

$$V_i(t) = (0.5 \cdot \tanh((U_i(t) - \theta)/\beta) + 0.5) \cdot \eta(t)$$

Here $\eta(t)$ is the optogenetic inactivation fraction, which tells us the fraction of this unit's output that is silenced by optogenetic inactivation in a time-dependent fashion (1 = no optogenetic inactivation). $\beta = 0.5$ controls the slope of the input–output relationship, and $\theta = 0.05$ controls the midpoint of the input–output function. The internal variables had dynamical equations:

$$\tau \cdot dU_i/dt = -U_i + W * V_i + input + \sigma \cdot dS$$

Where W is the network weight matrix, input is external inputs into the network and $\tau = 0.09$ s is a fixed time constant for each unit. S is a white noise Weiner process, scaled by noise amplitude parameter σ. W was parameterized by eight parameters that controlled the Pro self-weights sW_P and Anti self-weights sW_A, the horizontal weights hW_P between the two Pro units and hW_A between the two Anti units, the vertical weights vW_PA from the Anti unit to the Pro unit on the same side and vW_AP from the Pro unit to the Anti unit on the same side and the diagonal weights dW_PA from each Anti unit to the Pro unit on the opposite side and dW_AP from each Pro unit to the Anti unit on the opposite side. The external input into the network was given by:

$$input = E_{constant} + E_{Pro-bias} + E_{rule} + E_{choice-period} + E_{light}$$

$E_{constant}$ is the constant excitation to all units. Parameter $E_{Pro-bias}$ is the constant excitation to both Pro units but not to the Anti units. E_{rule} is the rule (task context) input, which is active only during the rule cue and delay periods and not during the choice period. On Anti trials, the two Anti units get task rule input $E_{Anti-rule}$, and, on Pro trials, the two Pro units get task rule input $E_{Pro-rule}$. Parameter $E_{choice-period}$ is excitation to all units only during the target period when a light stimulus is presented and animals are free to choose. Parameter E_{light} is excitation to both units on the side (L versus R) activated by the light stimulus, when the stimulus is active. Each trial was simulated numerically using the forward Euler method with timestep $dt = 0.024$ s, which we found to balance accuracy and computational speed. To encourage robust solutions, we trained the network on four different trial lengths. The task cue + delay period was either 1 s or 1.2 s, and the target period was either 0.45 s or 0.6 s. Individual trials of the same trial type and duration are differentiated by the noise samples generated by the additive Gaussian noise process. Model's choice on each trial is determined by the relative activation of the Pro units (see below). Therefore, although Pro units are directly linked to contralateral choices, Anti units are not directly linked to action and, therefore, can be either Ipsi-preferring or Contra-preferring.

Model cost function and frozen noise approach. The cost function has two terms $C = C_1 + C_2$. The first term C_1 penalizes model % correct accuracy that deviates from the target % correct accuracy. The second term C_2 penalizes weak model choices where output unit values are close together. The % correct accuracy for the C_1 term was defined as an average over N_F trials in each optogenetic condition. Each of the N_F trials differed from the others by having its own instantiation of neurons-by-timestep noise. This noise was kept frozen over iterations of the optimization procedure (thus rendering a cost function landscape that was constant across iteration steps). We reasoned that, for large enough N_F, and for a successfully trained network, this procedure would result in the targeted % correct accuracy even when the noise was no longer frozen, as successfully demonstrated in Fig. 6b,c.

C_1 Term: To create a fully differentiable choice readout, the model outputs the probability of the correct choice as: for a Pro trial where the light stimulus is on the left hemifield, the probability of a correct choice was given by $HitP = 0.5 \times (1 + tanh((V_{Pro-R} - V_{Pro-L})/\theta_1))$, and, for an Anti trial, $HitA = 0.5 \times (1 + tanh((V_{Pro-L} - V_{Pro-R})/\theta_1))$. θ_1 is a fixed sensitivity parameter. For each trial type, we penalized

the difference between the trial type's target hit percentage and the average hit percentage from the model across all trials of that type. The overall cost from this first term was the sum across trial types $C_1 = \sum_i \left(\overline{hitP}_i - TargetHitP_i\right)^2$.

C_2 Term: The C_1 term encourages the model to reach the target hit percentage on every trial rather than making strong choices on each trial, some right and some wrong, that average to the target hit percentage. Therefore, we introduced a second cost term that penalizes weak choices where the activation of the two Pro units are close. For a Pro trial where the light stimulus is on the left hemifield, $C_2 = -\beta_c(tanh((V_{Pro-R} - V_{Pro-L})/\theta_2))^2$; for an Anti trial, $C_2 = -\beta_c(tanh((V_{Pro-L} - V_{Pro-R})/\theta_2))^2$. θ_2 is a fixed parameter that controls the sensitivity of this term, and β_c is a fixed parameter controlling the strength of this term. We used the fixed parameter values $\theta_1 = 0.05$, $\theta_2 = 0.15$ and $\beta_c = 0.001$.

Model optimization. We initialized many different model solutions with random parameter values and a random seed for the random number generator to generate unique noise for each model solution. For each initialization, we minimized the cost function using constrained parabolic minimization.

Constrained parabolic minimization. At each step, the algorithm approximates the cost function locally using the Hessian matrix and gradient vector, which defines a parabolic surface. The minimization takes a step in the direction that minimizes the cost on this parabola with the step length equal to a constrained search radius. If the resulting step would increase the cost function, the step is not taken, the search radius is reduced and another step is attempted. As the search radius becomes smaller, this method converges to gradient descent.

Two-stage optimization. For each initialization, an initial minimization was done using $N_F = 50$ trials per condition. If this initial minimization passed a set of criteria, then a further minimization was done using $N_F = 1{,}000$ trials per condition. The initial criteria were that performance on Pro trials was greater than Anti trials, and Anti performance on delay period opto trials was worse than control or choice period opto trials. The final minimization terminated after 1,000 iterations or with parameter step tolerance of 1×10^{-12}. Optimizations with a final cost below −0.0001 were accepted as model solutions. We ended up with $n = 373$ unique model solutions.

Model analysis. We used singular value decomposition (SVD) as a dimensionality reduction on the dynamics of the networks. We simulated 200 trials for each model solution for each trial type (total 6 = Pro/Anti × control/delay-period-opto/choice-period-opto). Then, we computed the average trajectory for each unit in the model on correct and incorrect trials for each trial type. The average trajectories were concatenated into a model response vector (length $M = 4$ units × hit/error × Pro/Anti × control/delay/choice opto × T timesteps). We created response matrix (R) of response vectors for all model solutions (size $N \times M$). We used SVD to project R into a two-dimensional space (Fig. 7a). To compute the average task and choice decoding, we computed the d' sensitivity index for each solution and the decoding accuracy: % correct = NormalCDF(d'/sqrt(2)). When computing the distribution of choice d' values (Extended Data Fig. 8a), we used the activity of Pro and Anti model units in the middle of the choice epoch.

Schur decomposition analysis. The Schur decomposition factorizes the network connectivity matrix $W = MQM^T$, where M is a 4×4 matrix whose columns are orthogonal modes of W. Q is an upper triangular matrix. The diagonal of Q contains the eigenvalues associated with each column of M. The off-diagonal terms of Q describe the feed-forward interactions between each mode of M. Each Schur vector can be thought of as a functional mode in the network and has a corresponding eigenvalue that informs whether that mode gets amplified or diminished by the network[53–55]. We classified each Schur vector by the sign of each entry in the vector. For example, if the two Pro units have one sign, and the two Anti units have the opposite sign, we classify that vector as a 'task' mode. If the eigenvalue was complex-valued, we determined its stability by examining only the real-valued component. For a more detailed discussion, see the Supplementary Information.

Six-node SC model. Our six-node model (Extended Data Fig. 9) is a straightforward extension of the four-node model. We add an additional Anti unit (Anti-2) to each side. Anti-1 and Anti-2 receive the same external input. However, they have independent weights to and from the Pro units, to and from the contralateral units and independent self weights. In addition, we have bidirectionally independent weights between Anti-1 and Anti-2. Thus, Anti-1 and Anti-2 are allowed to be relatively independent. We used the same two-stage optimization procedure. Our cost function again depended only on the activity of the Pro nodes.

Statistics. Statistical analyses were conducted in MATLAB (2015, 2017) or Julia (1.51). No statistical methods were used to predetermine sample sizes, but our sample sizes are similar to those reported in previous publications[31]. We only analyzed neurons for which we had collected responses during at least 25 correct trials for each of the four possible task conditions, resulting in the analysis of 193 neurons (out of 215) in SC and 291 neurons (out of 331) in PFC. For population decoding analyses, performance was computed as the fraction of correct classifications over 500 resampling iterations. Because some of the neurons were recorded in different sessions, trials were always shuffled on each iteration to destroy any artificial trial-by-trial correlations. There was no assumption of data distribution for non-parametric tests. For other analyses, data distribution was assumed to be normal, but this was not formally tested. Statistical details for each analysis are specified in the respective part of the text. Data analyses were not performed blinded to the conditions of the experiments. See the Life Sciences Reporting Summary for additional information.

Reporting Summary. Further information on research design is available in the Nature Research Reporting Summary linked to this article.

Data availability

Processed behavioral, electrophysiological, optogenetic and video data are publicly available on GitHub: https://github.com/Brody-Lab/Proanti. Raw data are archived at Princeton University and available from the corresponding author upon reasonable request. Modeling data are publicly available on GitHub: https://github.com/carlosbrody/superior_colliculus_mutual_inhibition.

Code availability

All software used for behavioral training is available on the Brody lab website at http://brodylab.org/code/proanti-code. All custom data analysis and modeling codes are freely available on the corresponding GitHub repositories: https://github.com/Brody-Lab/Proanti (analysis) and https://github.com/carlosbrody/superior_colliculus_mutual_inhibition (modeling).

References

51. Pagan, M. & Rust, N. C. Dynamic target match signals in perirhinal cortex can be explained by instantaneous computations that act on dynamic input from inferotemporal cortex. *J. Neurosci.* **34**, 11067–11084 (2014).
52. Tibshirani, R. J. & Efron, B. An introduction to the bootstrap. *Monogr. Stat. Appl. Probab.* **57**, 1–436 (1993).
53. Goldman, M. S. Memory without feedback in a neural network. *Neuron* **93**, 715 (2017).
54. Murphy, B. K. & Miller, K. D. Balanced amplification: a new mechanism of selective amplification of neural activity patterns. *Neuron* **61**, 635–648 (2009).
55. Schaub, M. T., Billeh, Y. N., Anastassiou, C. A., Koch, C. & Barahona, M. Emergence of slow-switching assemblies in structured neuronal networks. *PLoS Comput. Biol.* **11**, e1004196 (2015).

Acknowledgements

We thank K. Osorio and J. Teran for animal and laboratory support. This work was funded by the Howard Hughes Medical Institute. C.A.D. was supported by a Howard Hughes Medical Institute predoctoral fellowship. C.A.D. and M.P. are supported by a Simons Collaboration on the Global Brain postdoctoral fellowship.

Author contributions

C.A.D. collected electrophysiological and optogenetics data. M.P. and C.A.D. analyzed electrophysiological data. C.A.D. analyzed the optogenetics data. M.P., A.T.P., C.D.B. and A.J.R. generated and analyzed modeling results. A.A. and C.D.K. carried out the acute optogenetics experiments. J.C.E. and C.D.K. played an advisory role on electrophysiological and optogenetics experiments, respectively. C.A.D., J.C.E. and C.D.B. conceived the project. C.A.D., M.P., A.T.P. and C.D.B. wrote the paper with comments from J.C.E. C.D.B. was involved in all aspects of experimental design and data analysis.

Competing interests

The authors declare no competing interests.

Additional information

Extended data is available for this paper at https://doi.org/10.1038/s41593-021-00865-x.

Supplementary information The online version contains supplementary material available at https://doi.org/10.1038/s41593-021-00865-x.

Correspondence and requests for materials should be addressed to C.A.D. or C.D.B.

Peer review information *Nature Neuroscience* thanks Gidon Felsen and the other, anonymous, reviewer(s) for their contribution to the peer review of this work.

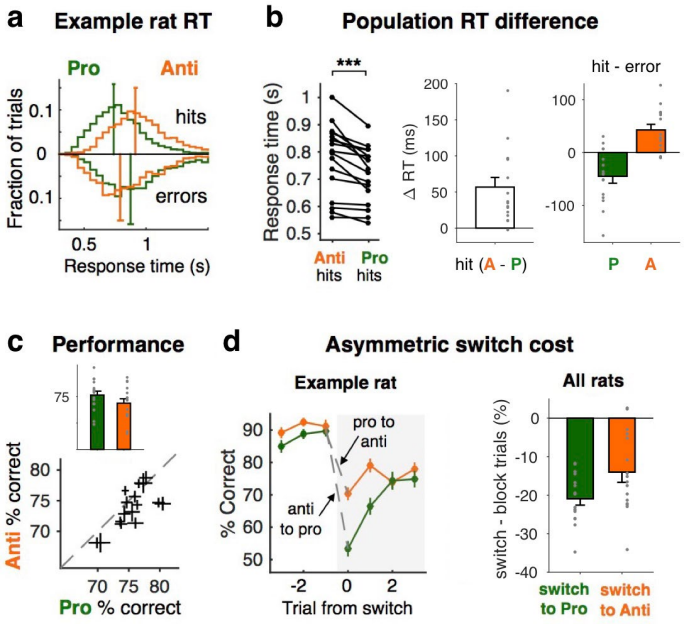

Extended Data Fig. 1 | Post-surgery performance for implanted rats. Asymmetries between Pro and Anti response time (RT), accuracy, and task switch cost in implanted rats. **a**, Normalized RT distributions of an example rat. Histograms of correct Pro (n = 3894 trials) and correct Anti (n = 3323) RTs are shown on top and error Pro (n = 1239 trials) and error Anti (n = 1161 trials) RTs are shown in the bottom. Each curve is normalized to have a total area of 1. Median RTs for Pro and Anti hits and errors are indicated by vertical bars; 95% confidence intervals across trials for each trial type are indicated by horizontal bars. **b**, RT summary of 16 individual rats (7 for SC and PFC neural recordings and 9 for optogenetic inactivation experiments). Left: median RTs for Anti hits and Pro hits for all rats (n = 16). ***$P = 4 \times 10^{-4}$, two-sided bootstrap test. Right: RT difference between Pro and Anti, hits and errors, averaged across all rats (n = 16). For each rat, the difference between median RTs of paired conditions was calculated. White bar shows the mean and s.e.m. across rats for Anti hit RTs minus Pro hit RTs, $P = 4 \times 10^{-4}$, two-sided bootstrap test. Green bar shows Pro hit RTs minus Pro error RTs, $P = 4 \times 10^{-4}$, two-sided bootstrap test. Orange bar shows Anti hit RTs minus Anti error RTs, $P = 4 \times 10^{-4}$, two-sided bootstrap test. **c**, Pro and Anti performance for individual rats (n = 16). Mean and s.e.m. of Pro and Anti performance are computed over sessions for each rat and plotted against each other. Average Pro (green) and Anti (orange) performance across rats was plotted in the upper left corner (n = 16). Pro versus Anti, $P = 0.003$, two-sided bootstrap test. **d**, Switch cost asymmetry. Left: percent correct as a function of trial number relative to a task block switch for one example rat. Each data point is the mean and s.e.m. across trials for Pro and Anti accuracy on three trials before and after the switch. Right: average accuracy switch cost for Pro trials ($P = 4 \times 10^{-4}$) and Anti trials ($P = 4 \times 10^{-4}$) across rats (n = 16). The cost of switching to Pro was larger than the cost of switching to Anti ($P = 0.002$), two-sided bootstrap tests.

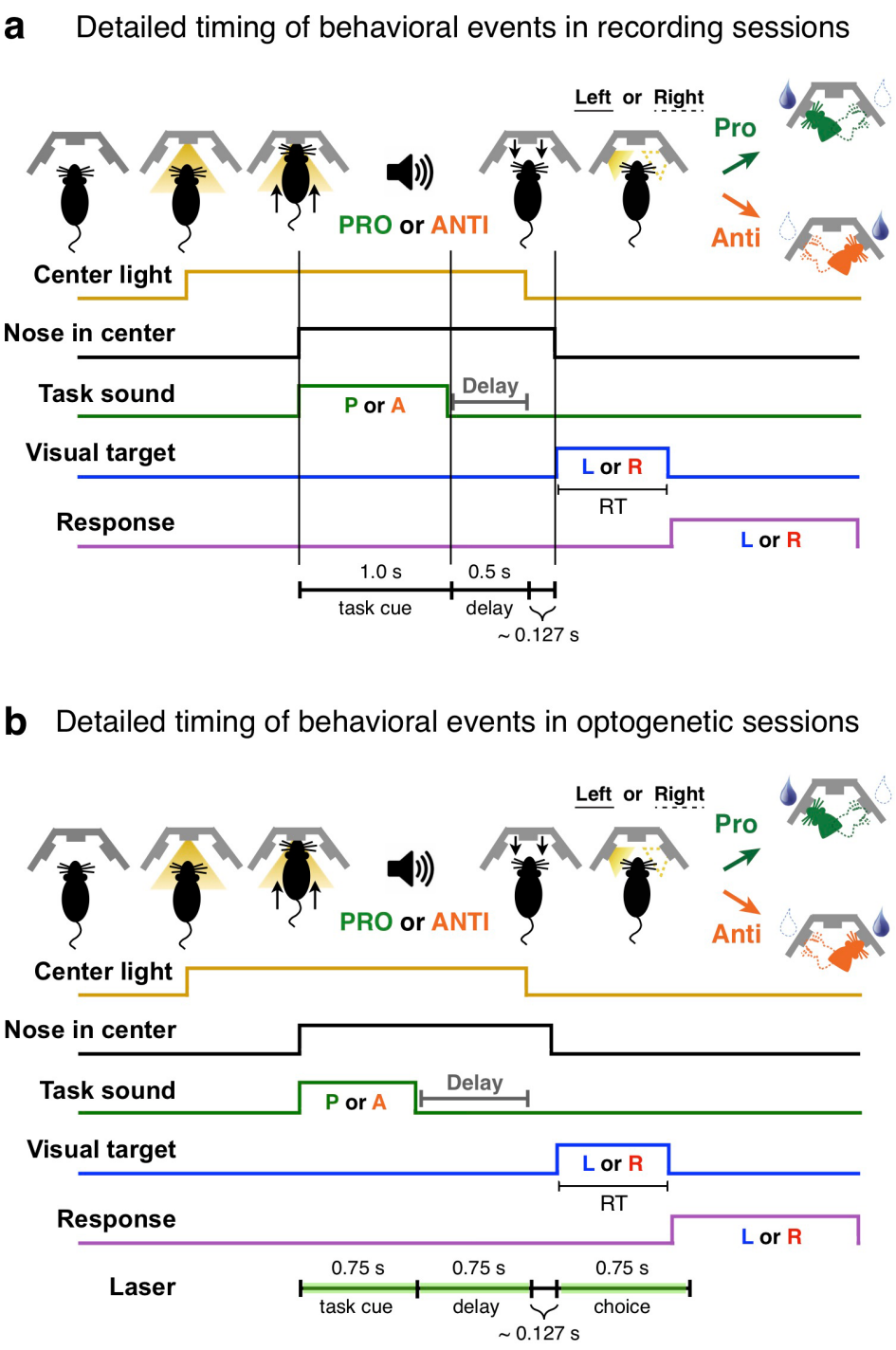

Extended Data Fig. 2 | Detailed timing of behavioral events in recording and optogenetic sessions. a, A light in the center port indicates that rats should nose poke there to initiate a trial and keep their noses there until the center light offset ("fixation" period). During the first 1 s of the fixation period, a Pro or Anti sound is played to indicate the current task, followed by a 500-ms silent delay. The center light is then turned off, indicating that the animal is now free to withdraw from the center port, and the moment it withdraws, a left or right light is turned on to indicate the target location. The temporal gap between fixation offset (that is, end of the delay period) and target stimulus onset was controlled by animals and was thus variable on each trial (mean = 127 ms after fixation offset). Reaction Time (RT) is defined as the time from target onset until side poke. The 3 vertical lines correspond to the vertical lines in Fig. 1–3. **b**, Similar to **a**, for optogenetic sessions. To ensure that all sub-trial optogenetic inactivation conditions have the same laser duration (750 ms, green shade), rats were trained on a modified version of the behavior where the task cue period and the delay period both lasted 750 ms. Choice period inactivation started at the onset of visual target and lasted 750 ms, covering the time it took animals to form and execute the orienting choice into the side poke (690.8 ± 39.1 ms, mean ± s.e.m. across animals' median RT in optogenetic inactivation sessions).

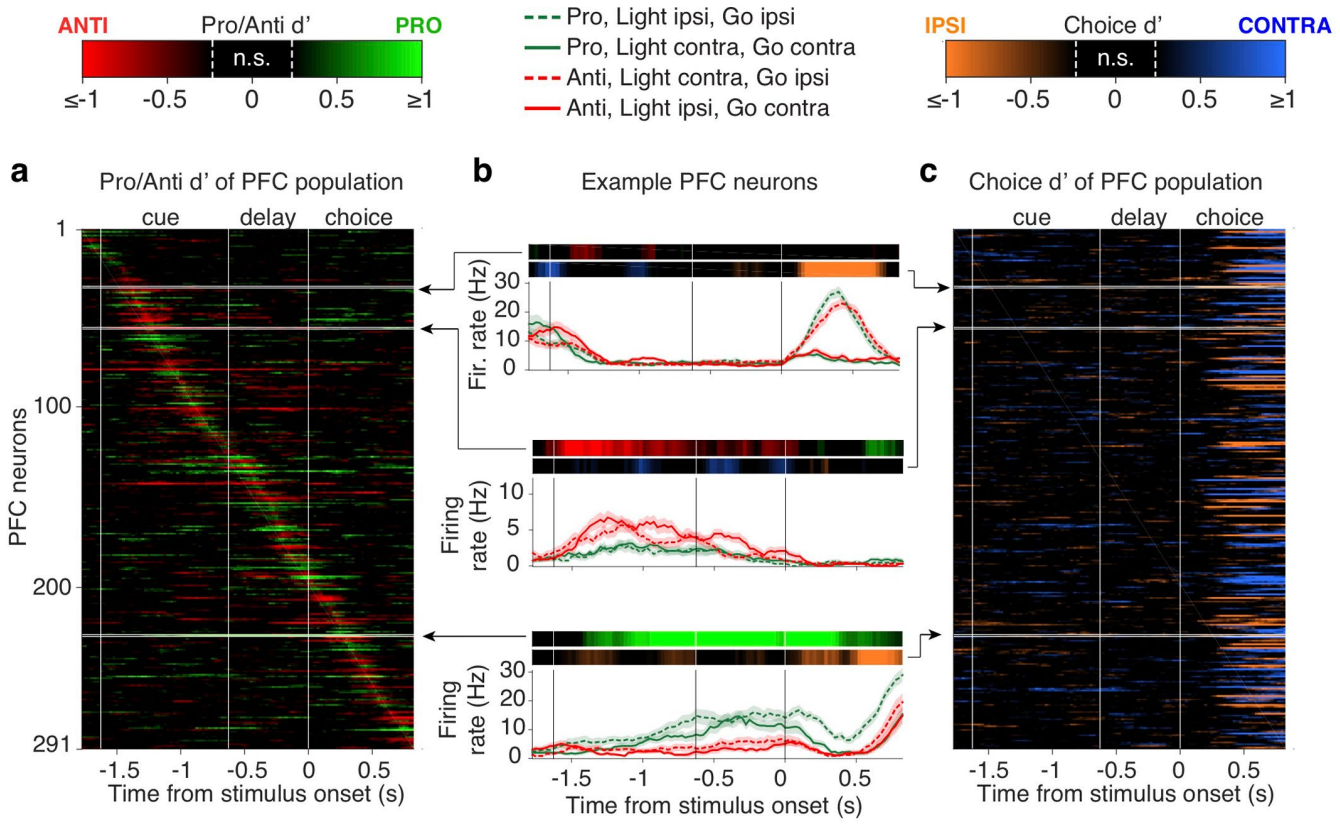

Extended Data Fig. 3 | Individual PFC neurons encode task and choice variables during flexible sensorimotor routing. a-c, Same as in Fig. 1c-e, for the PFC population (291 out of 331 total neurons).

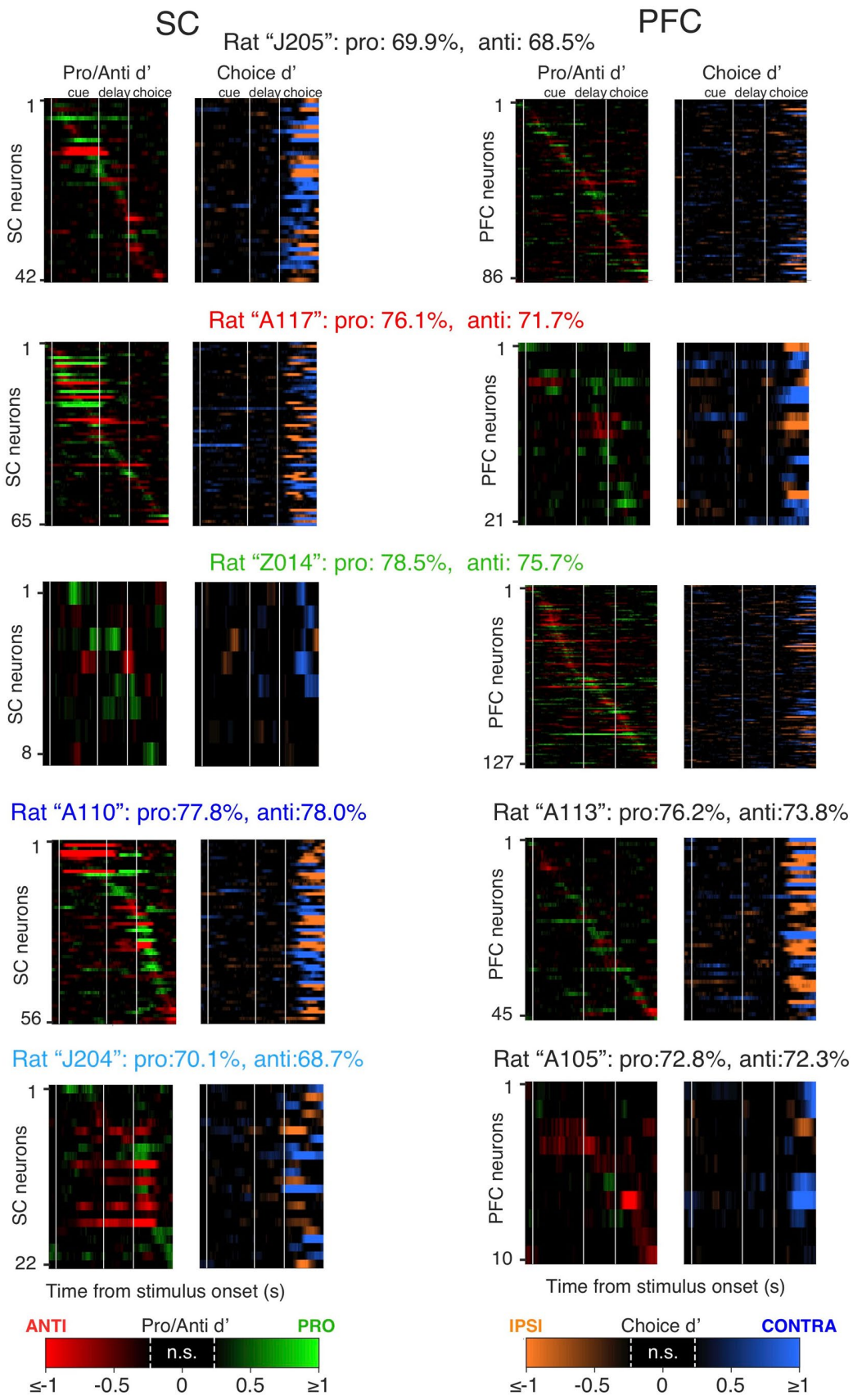

Extended Data Fig. 4 | Breakdown of electrophysiology results by rat. Similar to Fig. 1c,e, separated by recordings from individual rats. Mean performance on Pro and Anti trials during each rat's recording sessions are shown above each panel. Rat 'J205', 'A117', and 'Z014' had implants both in SC and in PFC. Rats with fewer than 20 neurons were excluded from this analysis.

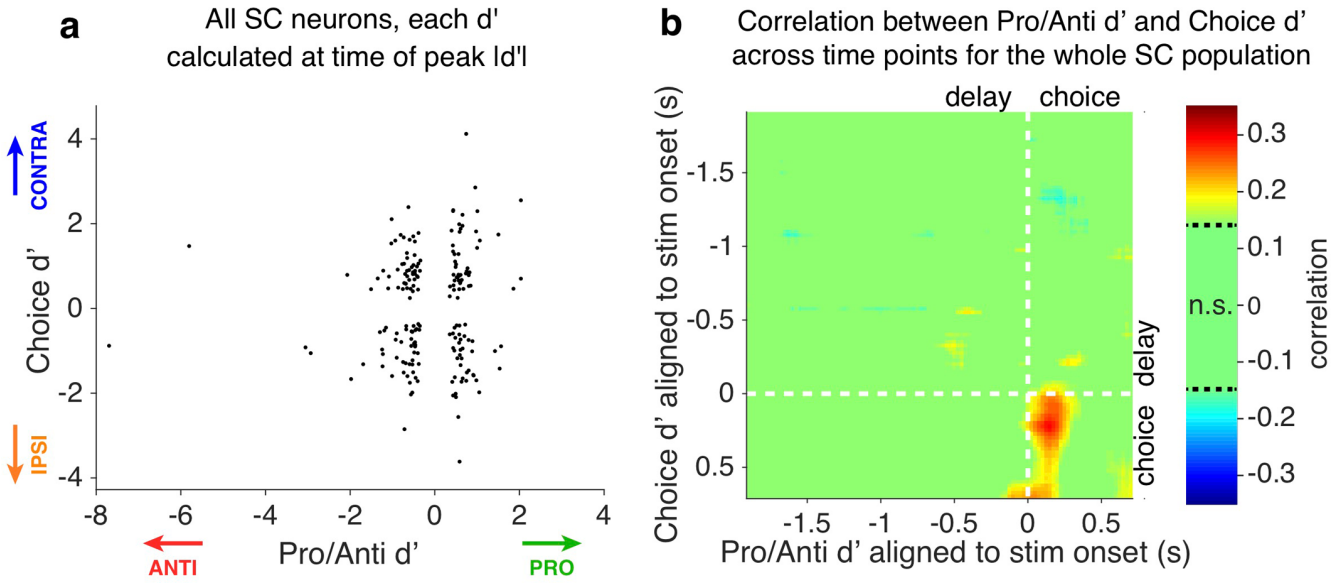

Extended Data Fig. 5 | Relationship between task context (Pro/Anti) and choice (Contra/Ipsi) d' across the SC population. a, For each SC neuron, the signed Pro/Anti d' computed at the time of peak Pro/Anti selectivity was plotted against the signed Choice d' computed at the time of peak Choice selectivity. No correlation is observed (Pearson's correlation coefficient r = 0.06, n = 193, $P = 0.3821$, t-test). **b**, Correlation between Pro/Anti d' and Choice d' for the whole SC population computed at all time points. The two black dashed lines in the color bar indicate the correlation values that are not significantly different from 0 ($P > 0.05$). The correlation is significantly different than 0 only at times shortly after the appearance of the target stimulus. Positive correlation corresponds to either a Pro (d' > 0) and Contra (d' > 0) preference or an Anti (d' < 0) and Ipsi (d' < 0) preference. Bin size = 250 ms, centered (that is, it includes spikes from ± 125 ms relative to the plotted timepoint.

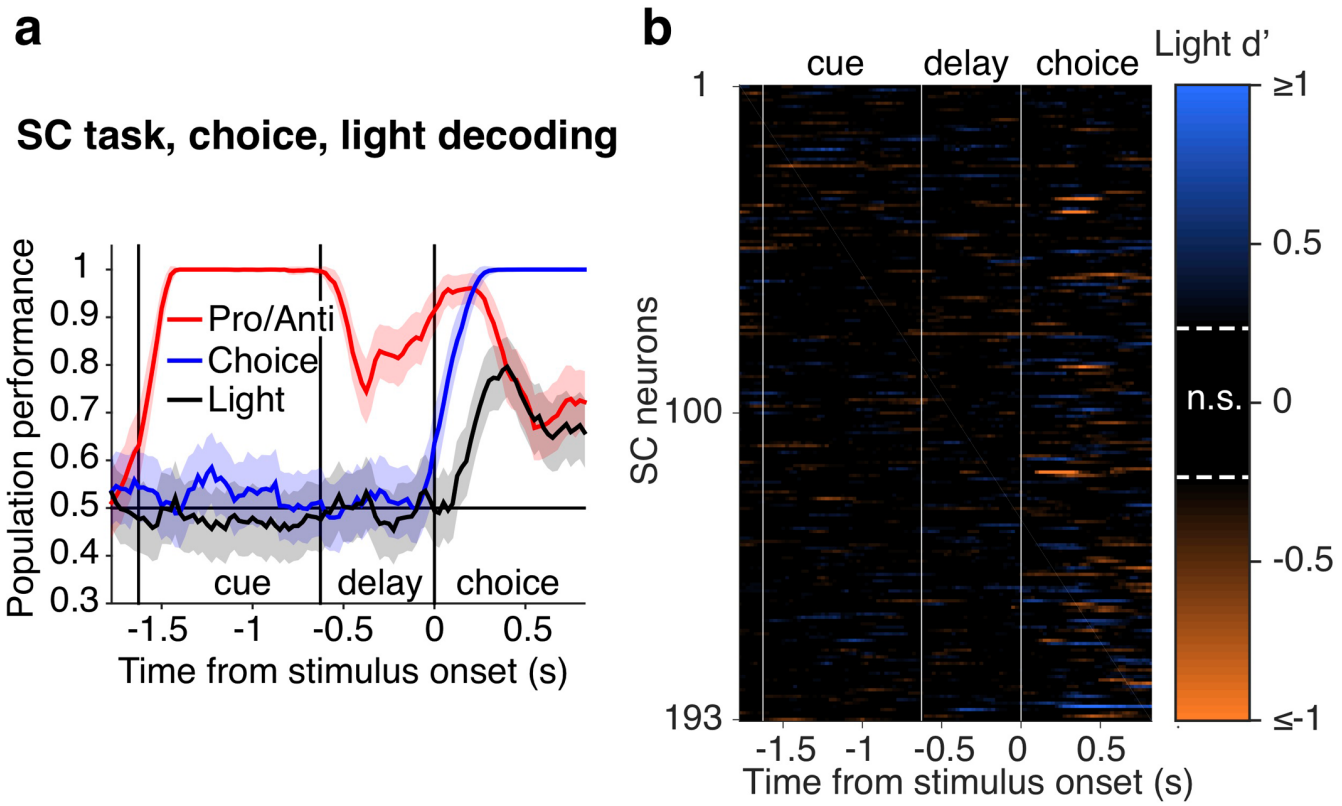

Extended Data Fig. 6 | Information regarding the side light stimulus in SC neurons. a, SC population decoding performance (mean ± s.d.) for linear classification of correct Pro versus Anti trials (task, red line), Go-Left versus Go-Right trials (choice, blue line), and Left-Light versus Right-Light trials (light stimulus, black line). Compared to the early and strong choice information in the SC population, linearly decodable information related to the light stimulus appeared later and weaker, suggesting that information being received by deep SC layer neurons about which side the Light is on is combined nonlinearly and very rapidly with context information, to produce early, linearly decodable information about choice. **b**, Matrix of light stimulus (left side light/ right side light) selectivity for the SC neural population, similar to Fig. 1e.

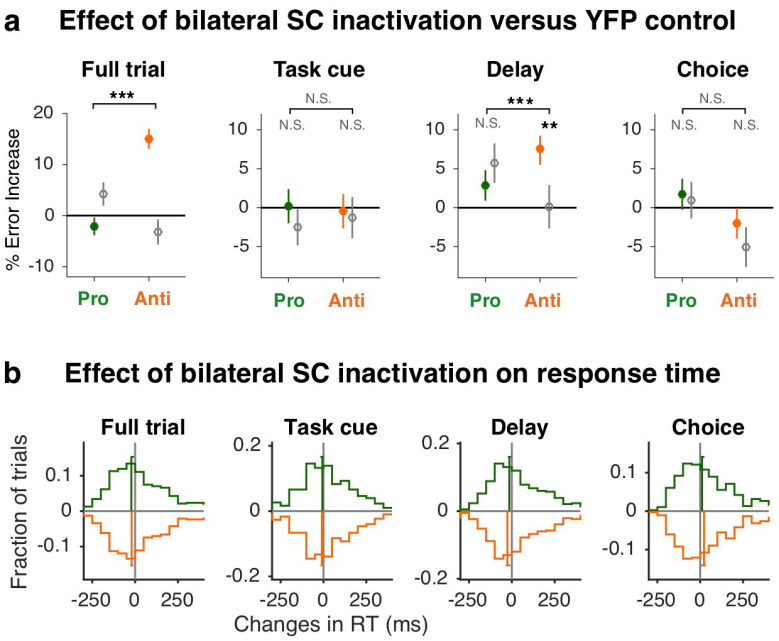

Extended Data Fig. 7 | Effect of bilateral SC inactivation and YFP control. a, Effect of full-trial and sub-trial inactivations of bilateral SC on Pro (green) and Anti (orange) error rate (mean and s.e.m.) compared to YFP controls (gray). Full-trial: n = 662, 615 for Pro and Anti inactivation trials; n = 362, 322 for Pro and Anti control trials. $^{***}P = 4 \times 10^{-4}$, two-sided permutation test. Task cue: n = 413, 401 for Pro and Anti inactivation trials; n = 290, 271 for Pro and Anti control trials. Delay: n = 562, 527 for Pro and Anti inactivation trials; n = 315, 260 for Pro and Anti control trials. $^{***}P = 4 \times 10^{-4}$; $^{**}P = 0.0012$, two-sided permutation tests. Choice: n = 547, 506 for Pro and Anti inactivation trials; n = 319, 261 for Pro and Anti control trials. All paired statistics shown here are computed using a two-sided permutation test, shuffled 5000 times. **b**, Effect of full-trial and sub-trial inactivations of bilateral SC on response time (RT). For each behavioral session, a median RT on non-stimulated control trials is calculated and subtracted from the RTs on inactivation trials, and these normalized RT changes due to inactivation are plotted here. Each curve is normalized to have a total area of 1. Vertical bars show the median RT changes for correct Pro and Anti trials; s.e.m. across trials for each trial type are indicated by horizontal bars. A shift to the right indicates slowing due to inactivation and a shift to the left indicates speeding.

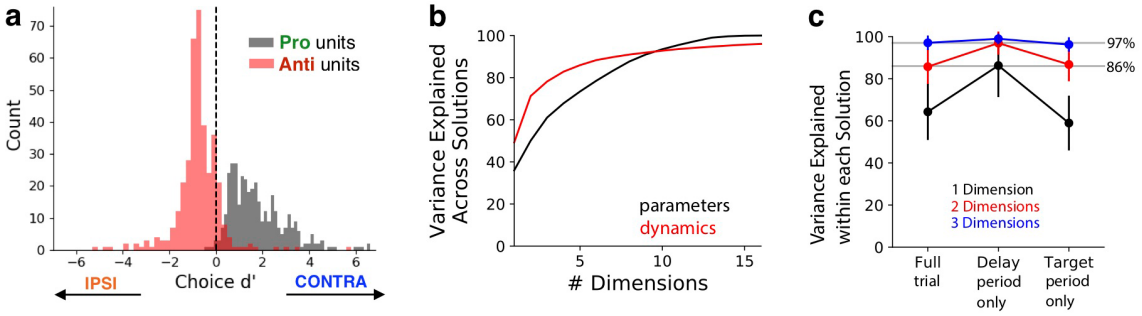

d

functional modes	All	Side	Task	Diagonal
% of solutions with mode	100	100	100	100
% of modes with positive eigenvalue	60.3	50.9	94.9	98.4

Extended Data Fig. 8 | Variability across model solutions in dynamics and parameters, and common functional properties. a, Distribution of choice preference (d') for Pro and Anti model units from 373 individual model solutions during the choice period (Methods). Note that although most Anti units (red shading) were Ipsi-preferring, we also observed Anti/Contra-preferring units (red shaded counts to the right of zero), similar to the SC neural data (Fig. 4). In contrast, all Pro units (gray shading) were Contra-preferring. **b**, The dimensionality of parameters across model solutions, and of dynamics across model solutions (n = 373 solutions). Eight SVD dimensions are required to explain 90% of the variance in dynamics across model solutions. Ten PCA dimensions are required to explain 90% of the variance in parameters across model solutions. **c**, Variance explained by each dimension of PCA performed on each model solution's dynamics. Full trial: PCA computed on all time points. Delay period only: PCA computed only during the delay period. Target period only: PCA computed only during the target period. Mean ± s.d across 373 model solutions. **d**, The connectivity matrix of each model solution was analyzed via the Schur Decomposition (Methods). All solutions (n = 373) contained one of each of the following functional modes: All, Side of brain, Task, and Diagonal. The percentage of solutions with positive eigenvalues for each mode is reported.

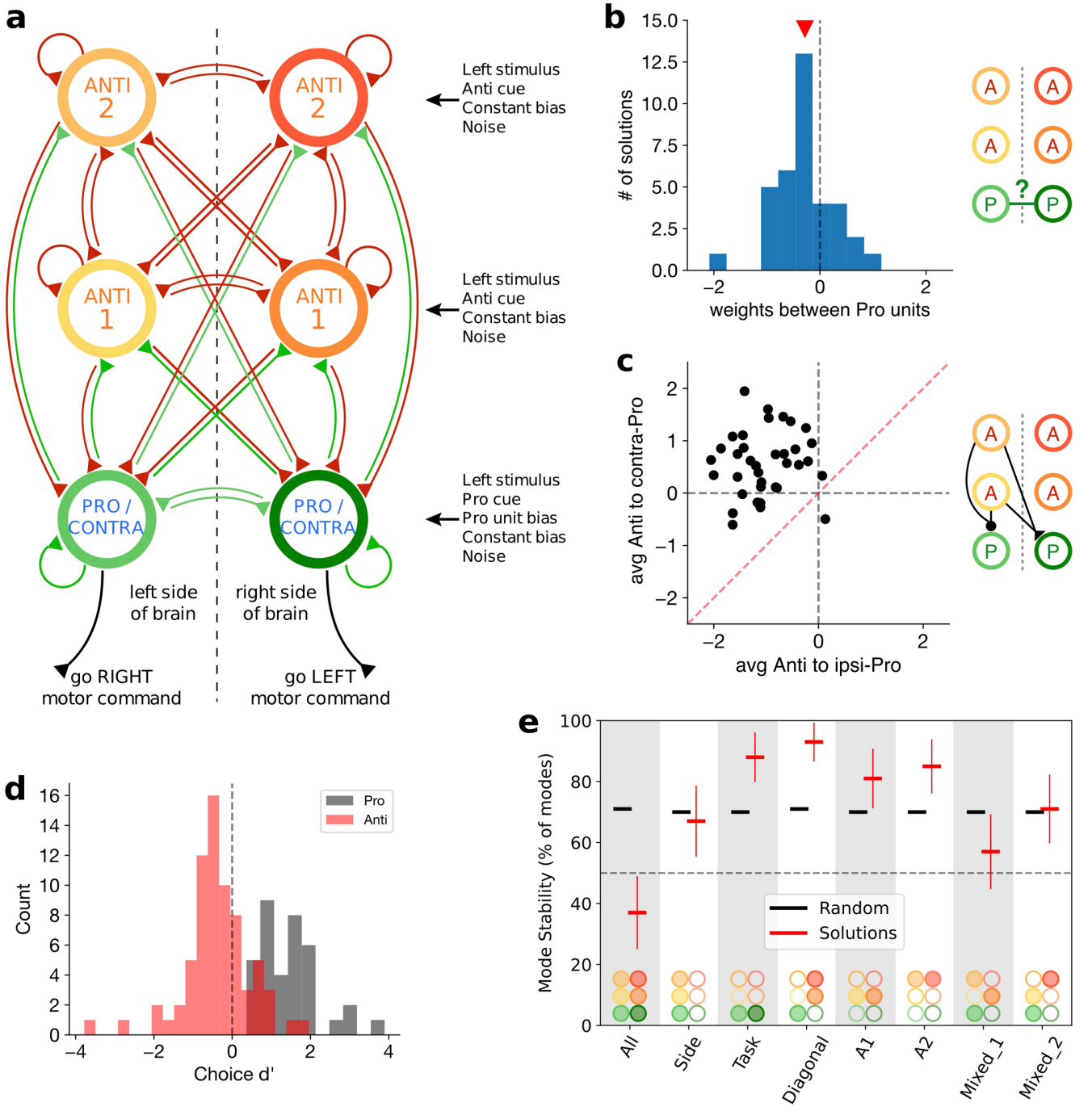

Extended Data Fig. 9 | A 6-node SC model replicates results from the 4-node SC model. a, Schematic of the 6-node SC model, in which each hemisphere contains two Anti pools and one Pro pool. **b**, Format and results similar to Fig. 7e. Histogram of horizontal weights between the two Pro units (as illustrated by the insert cartoon) for all 36 six-node model solutions. Red arrow marks average value across solutions. Solutions do not require inhibitory weights between the two Pro/Contra pools. **c**, Format and results similar to Fig. 7c. Scatter plot of diagonal weights (from Anti units to the Pro unit on the opposite hemisphere) against vertical weights (from Anti units to the Pro unit on the same hemisphere), for all model solutions. Each dot represents the average weights from the two Anti units in a solution. Red line marks unity. **d**, Format and results similar to Extended Data Fig. 8a. Histogram of choice d' for Pro and Anti nodes during the choice period (n = 36 model solutions). We observed both Anti/Ipsi and Anti-Contra-preferring units, with a majority of Anti/Ipsi units, as in the experimental data. **e**, Similar to Extended Data Fig. 8d. Percentage of model solutions with positive eigenvalues for each Schur mode type, based on Schur Decomposition analysis of the connectivity matrix. The solution networks (n = 36 solutions, red, mean ± 95% CI) are compared against 10,000 random networks (black) with the same symmetry and parameter value constraints. Dashed line indicates results from 10,000 random networks with the same symmetry, but not the parameter value constraints.

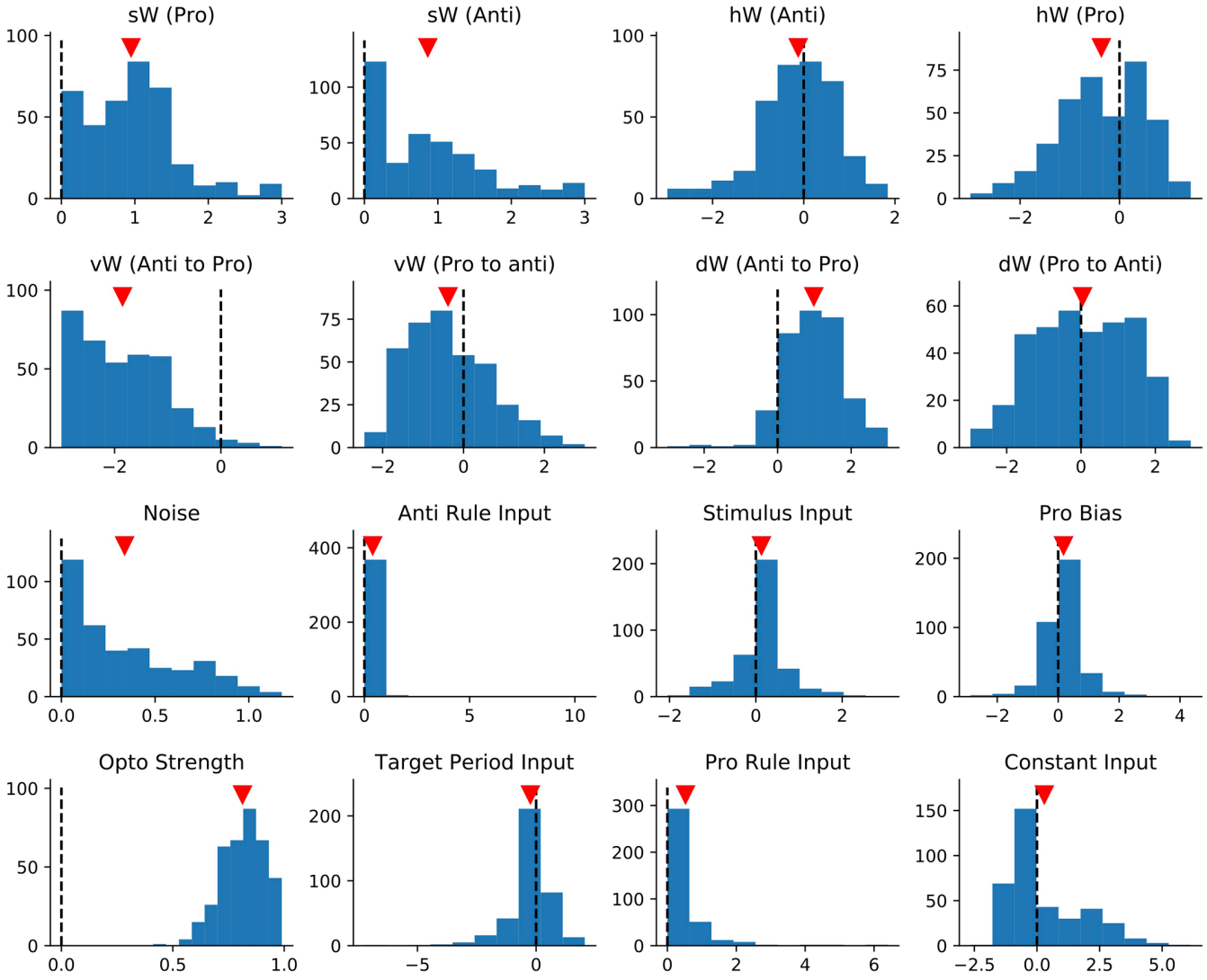

Extended Data Fig. 10 | Distributions of parameters across all model solutions. The distribution of parameter values across all solutions (n = 373) is plotted for each of the 16 free parameters (Methods). Vertical dashed line marks zero for reference. Red arrow marks average parameter value across solutions. The weight parameters determined the connectivity matrix between units. The noise parameter was the variance of white noise added to each unit on each time step. The Pro and Anti rule input weights determined the strength of the task context inputs to either the Pro or Anti units. The stimulus input determined the weight of the stimulus to either the Left or Right units. The Pro bias term was a constant input to only the Pro units. The target period input was a constant input to all nodes, only during the target period. The constant input was a bias term during all time points for all units. The opto strength was the fraction of each node's output that was transmitted to the other nodes during inactivations; a strength of 1 is no inactivation, a strength of 0 is complete inactivation.

nature research

Corresponding author(s): Chunyu A. Duan and Carlos D. Brody

Last updated by author(s): Mar 29, 2021

Reporting Summary

Nature Research wishes to improve the reproducibility of the work that we publish. This form provides structure for consistency and transparency in reporting. For further information on Nature Research policies, see our Editorial Policies and the Editorial Policy Checklist.

Statistics

For all statistical analyses, confirm that the following items are present in the figure legend, table legend, main text, or Methods section.

n/a	Confirmed	
☐	☒	The exact sample size (*n*) for each experimental group/condition, given as a discrete number and unit of measurement
☐	☒	A statement on whether measurements were taken from distinct samples or whether the same sample was measured repeatedly
☐	☒	The statistical test(s) used AND whether they are one- or two-sided *Only common tests should be described solely by name; describe more complex techniques in the Methods section.*
☒	☐	A description of all covariates tested
☐	☒	A description of any assumptions or corrections, such as tests of normality and adjustment for multiple comparisons
☐	☒	A full description of the statistical parameters including central tendency (e.g. means) or other basic estimates (e.g. regression coefficient) AND variation (e.g. standard deviation) or associated estimates of uncertainty (e.g. confidence intervals)
☐	☒	For null hypothesis testing, the test statistic (e.g. *F*, *t*, *r*) with confidence intervals, effect sizes, degrees of freedom and *P* value noted *Give P values as exact values whenever suitable.*
☒	☐	For Bayesian analysis, information on the choice of priors and Markov chain Monte Carlo settings
☒	☐	For hierarchical and complex designs, identification of the appropriate level for tests and full reporting of outcomes
☐	☒	Estimates of effect sizes (e.g. Cohen's *d*, Pearson's *r*), indicating how they were calculated

Our web collection on statistics for biologists contains articles on many of the points above.

Software and code

Policy information about availability of computer code

Data collection	All software used for behavioral training is available on the Brody lab website at http://brodylab.org/code/proanti-code.
Data analysis	For population-level decoding analysis, we employed a Support Vector Machine algorithm using the LIBSVM library (v3.17; https://www.csie.ntu.edu.tw/~cjlin/libsvm/). For modeling, we used Forward-mode automatic differentiation (v0.10; Revels et al., 2016, arXiv:1607.07892). All other analysis codes used in this study were custom codes written in MATLAB (2015, 2017) or Julia (1.51). Software used for data analysis, as well as raw and processed data, are available in these 2 github repositories: https://github.com/carlosbrody/superior_colliculus_mutual_inhibition; https://github.com/Brody-Lab/Proanti.

For manuscripts utilizing custom algorithms or software that are central to the research but not yet described in published literature, software must be made available to editors and reviewers. We strongly encourage code deposition in a community repository (e.g. GitHub). See the Nature Research guidelines for submitting code & software for further information.

Data

Policy information about availability of data

All manuscripts must include a data availability statement. This statement should provide the following information, where applicable:

- Accession codes, unique identifiers, or web links for publicly available datasets
- A list of figures that have associated raw data
- A description of any restrictions on data availability

Processed behavioral, electrophysiological, optogenetic, and video data are publicly available on github: https://github.com/Brody-Lab/Proanti. Raw data are archived at Princeton University and available from the corresponding author upon reasonable request. Modeling data are publicly available on github: https://github.com/carlosbrody/superior_colliculus_mutual_inhibition.

Field-specific reporting

Please select the one below that is the best fit for your research. If you are not sure, read the appropriate sections before making your selection.

☒ Life sciences ☐ Behavioural & social sciences ☐ Ecological, evolutionary & environmental sciences

For a reference copy of the document with all sections, see nature.com/documents/nr-reporting-summary-flat.pdf

Life sciences study design

All studies must disclose on these points even when the disclosure is negative.

Sample size	No statistical methods were used to pre-determine sample sizes, but our sample sizes are similar to those reported in previous publications (Hanks et al., 2015). We used 24 adult male Long-Evans rats (Taconic) for the experiments presented in this study. Of these, 12 rats were used for electrophysiology recordings, and 12 rats were implanted with optical fibers for the optogenetic inactivation and YFP control experiments. All statistical tests were made between groups with similar sample sizes.
Data exclusions	No data has been excluded, except for the electrophysiological analysis, in which from the total of 546 single units recorded in the superior colliculus and prelimbic cortex, we only analyzed neurons for which we had collected responses during at least 25 correct trials for each of the four possible task conditions. These neurons summed to a total of 484. The rationale behind this exclusion is to only include neurons in recording sessions where there were enough trials in each condition (Pro correct, Anti correct, Pro error, Anti error) for analyses (see Pagan et al., 2014).
Replication	Electrophysiological recordings were conducted in multiple rats for each brain region recorded (5 rats for SC, 6 rats for mPFC, and 5 rats for FOF), and we observed consistent results across individual rats. Of these implanted rats, 4 rats had both SC and mPFC recordings, controlling for behavioral differences across recording sessions. Optogenetic inactivation experiments were carried out from 9 rats, over multiple sessions, and all types of inactivations were randomly interleaved for each session. Modeling analyses were conducted over 373 model solutions. All main conclusions from the 4-node models were replicated in a separate set of 6-node models with different model architecture.
Randomization	All subjects were randomly allocated into experimental groups.
Blinding	All behavioral and neural responses in our experiments were objectively measured by automated hardware and software system that do not require human intervention, and therefore were not blinded to investigators.

Reporting for specific materials, systems and methods

We require information from authors about some types of materials, experimental systems and methods used in many studies. Here, indicate whether each material, system or method listed is relevant to your study. If you are not sure if a list item applies to your research, read the appropriate section before selecting a response.

Materials & experimental systems

n/a	Involved in the study
☒	☐ Antibodies
☒	☐ Eukaryotic cell lines
☒	☐ Palaeontology and archaeology
☐	☒ Animals and other organisms
☒	☐ Human research participants
☒	☐ Clinical data
☒	☐ Dual use research of concern

Methods

n/a	Involved in the study
☒	☐ ChIP-seq
☒	☐ Flow cytometry
☒	☐ MRI-based neuroimaging

Animals and other organisms

Policy information about studies involving animals; ARRIVE guidelines recommended for reporting animal research

Laboratory animals	Male, long–Evans rats (Rattus norvegicus) between the ages of 6 and 24 months were used for this study.
Wild animals	The study did not involve the wild animals.
Field-collected samples	The study did not involve the Field-collected samples from the filed.
Ethics oversight	All animal use procedures were approved by the Princeton University Institutional Animal Care and Use Committee and carried out in accordance with NIH standards.

Note that full information on the approval of the study protocol must also be provided in the manuscript.